

Ribbon curling

Chris Prior ^{*}, Julien Moussou [†], Buddhapriya Chakrabarti ^{*}, Oliver E. Jensen [‡] and Anne Juel [‡]

^{*}University of Durham, Durham, UK, [†]University of Manchester, Manchester, UK, and [‡]Ecole Normale Supérieure, Paris, France

Submitted to Proceedings of the National Academy of Sciences of the United States of America

The procedure of curling a ribbon by running it over a sharp blade is commonly used when wrapping presents. Despite its ubiquity, a quantitative explanation of this everyday phenomenon is still lacking. We address this using experiment and theory, examining the dependence of ribbon curvature on blade curvature, the longitudinal load imposed on the ribbon and the speed of pulling. Experiments in which a ribbon is drawn steadily over a blade under a fixed load show that the ribbon curvature is generated over a restricted range of loads, the curvature/load relationship can be non-monotonic, and faster pulling (under a constant imposed load) results in less tightly curled ribbons. We develop a theoretical model that captures these features, building on the concept that the ribbon under the imposed deformation undergoes differential plastic stretching across its thickness, resulting in a permanently curved shape. The model identifies factors that optimize curling and clarifies the physical mechanisms underlying the ribbon's nonlinear response to an apparently simple deformation.

elasticity | plasticity | mechanics | stress relaxation

Abbreviations: None

Classification: Physical sciences; applied physical sciences

Significance statement: The forming of thin film structures through intrinsic stress relaxation is an important design tool to create flexible shapes such as rolls, spirals and origamis from the macro- to the nano-scale. We exploit the everyday process inspired from gift wrapping, of curling an initially straight ribbon by pulling it over a blade, to probe the mechanical shear response of thin polymer sheets. Experiments show that curling occurs over a limited range of loads applied to the ribbon, with the curl radius reaching a maximum at intermediate loads. A theoretical model reveals several patterns of irreversible yielding across the ribbon, and the dependence of curl radius on pulling speed shows that the stress relaxes dynamically as the ribbon passes over the blade.

Bend a ribbon over a scissor blade by pressing it firmly down with your thumb, and pull the ribbon over the blade. This is the commonplace method for curling ribbons for decorative gift-wrapping. But what is the mechanism by which ribbon coils are produced? How does the coil depend on the speed of pulling, the shape of the blade and the tension in the ribbon? We address these questions using a combination of experiments and theory, showing how curling arises via a plastic deformation that is regulated by both spatial and temporal effects.

A familiar example of curvature generation in thin materials is the bimetallic strip (or thermocouple), for which curvature arises from differential thermal expansion of two adherent layers of elastic material; the strip bends on heating but recovers its initially straight configuration on cooling to its original temperature [1]. Some biological materials exploit the same principle, but with expansion driven by water fluxes: reversible differential expansion arises in bilayer plant tissues such as the anther [2], pine cone scale [3] or wet paper [4], whereas irreversible differential cell expansion drives the bending of roots and shoots [5].

In contrast to these examples, a ribbon is a homogeneous material, at least prior to curling. Further, the curling deformation is permanent, pointing to the fact that a part of the material undergoes yield during the deformation process. Accordingly, the experiments we report below reveal that a threshold load must be applied in order to induce curling, while excessive loading may prevent curling or even tear the ribbon completely. Similar plastic deformation is inadvertently applied by rolling up paper scrolls for storage, resulting in curled edges that have plagued Chinese scrolls for centuries [6]; however, the generation of this widthwise curvature is negligible in our narrow ribbons. Unlike prior studies of the bending of elasto-plastic beams under a stationary transverse load [7, 8], our study addresses dynamic stress relaxation effects and shows how curling is modulated by an axial load. Our work also differs from studies of bending of soft visco-plastic threads, for which yield surfaces are orthogonal, rather than parallel, to the thread axis [9].

Somewhat surprisingly, our experiments show that the maximum ribbon curvature is typically generated at an intermediate load. We develop a theoretical model in order to explain the non-monotonic relationship between curvature and load. The central idea is that, as a material element of ribbon passes onto the blade and is forced into a configuration with high curvature, it undergoes yield in a region near its outermost surface; however, as the ribbon element leaves the blade, there can be a further deformation involving irreversible stretching of the ribbon close to its inner surface. The former deformation promotes curling, the latter reduces it. Curvature is modulated further by the pulling speed, which determines how the transit time of the element over the blade compares to the stress relaxation time of the material. Our model captures the key elements of this robust phenomenon and demonstrates how the curling process provides insight to the shear response of thin stiff sheets of polymer that yield under relatively low loads.

Results

Experimental results. A schematic side-view diagram of the experimental apparatus is shown in Fig. 1A. A polymer ribbon [10] of thickness $H^* = 100 \pm 3 \mu\text{m}$ and width $W^* = 10.0 \pm 0.3 \text{ mm}$, made from PVC transparency film, is pulled steadily over a blade at a prescribed rate (by attaching the ribbon to a rotating drum) and under a prescribed load (provided by a weight attached to one end). We used machined blades

Reserved for Publication Footnotes

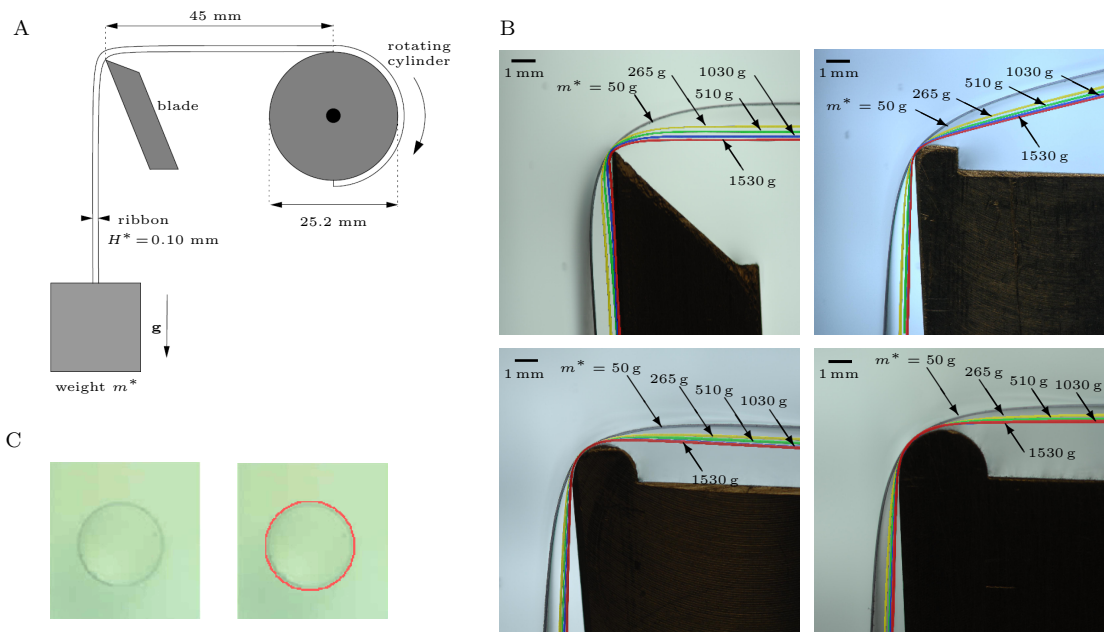


Fig. 1. Experimental setup for ribbon curling. (A) Side-view schematic diagram of the experimental apparatus. (B) Side-view photographs of the experimental ribbon shapes bending over the blade for different ribbon tensions imposed by hanging weights $m^* = 50$ g (grey), 265 g (yellow), 510 g (green), 1030 g (blue) and 1530 g (red) as shown in (A). From top left to bottom right: sharp blade, blade radius $R^* = 1$ mm, $R^* = 1.5$ mm and $R^* = 2$ mm. In all cases except for $R^* = 1$ mm, the rotating cylinder and top edge of the blade are positioned at the same height. For $R^* = 1$ mm (top right image), the cylinder position is higher than the blade so that the ribbon under tension is oriented with an angle of 14° with respect to the horizontal direction, and the contact area of the ribbon with the blade is reduced. (C) Measurement of the curl radius: top-view photograph of a single curl where the edge of the ribbon rests on a perspex sheet, and superposition of the ribbon outline obtained using edge-finding and the Hough transform onto the curled ribbon.

with radius of curvature $R^* = 1, 1.5$ and 2 mm, and a fourth ‘sharp’ blade with a much higher curvature ($R^* < 0.1$ mm). Pulling imprints a permanent curvature on the ribbon, which is measured after the ribbon is removed from the blade (Fig. 1C) (see *SI Appendix*).

Images of the experimental ribbon configurations over each blade are shown in Fig. 1B for loads in the range $50 \text{ g} \leq m^* \leq 1530 \text{ g}$. In each case, the ribbon’s resistance to bending led to slightly different ribbon geometries over the blade for increasing loads. This was most significant for the sharp blade where the ribbon configuration varied significantly over the entire range of loads, and could not conform to the radius of curvature of the blade. Measurable changes in configuration were also found for the $R^* = 1$ mm blade over this range of loads; for $R^* = 1.5$ mm and $R^* = 2$ mm, the ribbon approximately adopted the curvature of the blade at $m^* = 1030$ g and $m^* = 510$ g, respectively, so that the geometry of the ribbon remained unchanged for higher loads.

Dimensional permanent curvature measurements are shown using symbols in Fig. 2A, as a function of axial load applied to the ribbon for each of the four blades. The data corresponding to experiments with the sharp and $R^* = 1$ mm blades exhibit a characteristic triangular shape, where curvature increases approximately linearly with increasing load to a maximum in curvature that is larger the sharper the blade. The curvature then decreases monotonically upon further increase of the load. In both cases, the maximum load applied was determined by the smallest value of curvature that could be reliably measured at high loads. In contrast, for $R^* = 1.5$ mm and 2 mm, the curvature increased monotonically up to a maximum load, beyond which the ribbon ruptured. For $R^* = 1.5$ mm, the curvature appears to have reached a maximum, whereas for $R^* = 2$ mm, only a small in-

crease in curvature could be observed before the load exceeded its threshold value for rupture. The threshold load was found to increase as the curvature of the blade was reduced (Fig. 2A). The four sets of experimental data also suggest that a critical load needs to be exceeded in order for the ribbon to curl, and this critical load increases significantly with reduction in blade curvature. Hence, the modest loads required to bend the ribbon over the sharp and 1 mm blades meant that the ribbon geometry varied with load over the entire range investigated (Fig. 1B), whereas the larger loads required to bend the ribbon over the $R^* = 1.5$ mm and 2 mm blades exceeded the values at which the ribbon geometry reached a constant configuration. The effect on ribbon curling of the pulling speed was investigated for $R^* = 1$ mm and two applied loads ($m^* = 960$ and 689 g). Experimental data shown with symbols in Fig. 2B indicate that the curvature of the ribbon curl decreases monotonically with linear pulling speed.

In order to inform comparison with the theoretical model, the material properties of the PVC ribbon were measured with uniaxial tensile tests performed using an Instron 3345 (L2957) universal testing system. The Young’s modulus E^* was determined by linear least-square fit of average stress-strain curves measured in the elastic regime to take a value of $E^* = 2.5 \pm 0.4$ GPa. The viscoplastic behaviour of the material was investigated with creep experiments, where stress was applied to six different ribbon samples in successive step changes of variable magnitude. The average rate of plastic strain creep was determined with a linear fit to the time variation of strain data following each step change in applied stress. The average strain rate is shown in Fig. 2C as a function of applied stress, where each symbol indicates experiments performed on an individual ribbon sample. The strain rate is approximately zero below a critical yield stress, and increases approximately

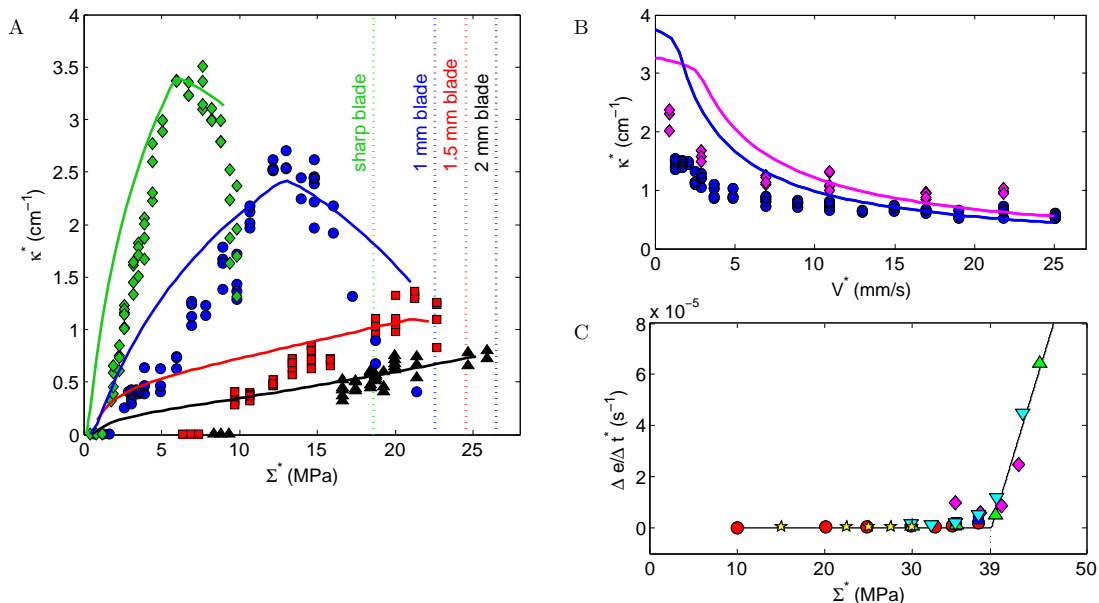


Fig. 2. Comparison between experimental measurements and theoretical predictions. (A) Symbols show experimental measurements of the permanent curvature of the curled ribbon as a function of stress applied to the end of the ribbon (see Fig. 1A), for the four blades: sharp blade (green diamond), $R^* = 1$ mm (blue circle), $R^* = 1.5$ mm (red square) and $R^* = 2$ mm (black triangle). In all cases, curling is observed above a threshold value of the applied load which depends of the radius of curvature of the blade. For the sharp blade, $R^* = 1$ mm and $R^* = 1.5$ mm, the curvature increases approximately linearly above the threshold load to a maximum value that decreases as R^* is increased. The curvature then decreases approximately linearly with applied load, and for $R^* = 1$ mm, the minimum values of curvature measurable experimentally are recovered. The vertical dotted lines correspond to the typical loads at which the ribbon ruptured on the blade. For $R^* = 1.5$ mm, the rupture load is very close to the maximum of curvature, so the decrease of curvature with load cannot be observed. For $R^* = 2$ mm, the curvature does not show evidence of a maximum below the rupture load. The pulling speed is $V^* = 4.9$ mm/s. Lines show model predictions using parameters $V^* = 4.9$ mm/s and $E^* = 2.5$ GPa. Values of the yield stress and plastic relaxation time were adjusted to $Y^* = 28, 30, 31, 40$ MPa and $t_p^* = 0.15, 0.18, 1.0, 0.9$ s for the sharp, 1mm, 1.5mm and 2mm blades respectively. The angles at which the ribbon is pulled are similar to those shown in Fig. 1B. (B) Symbols show experimentally measured curvature as a function of pulling speed V^* for two different weights: $m^* = 689$ g (blue circles) and $m^* = 960$ g (cyan diamonds), using the blade with radius $R^* = 1$ mm. The curvature decreases approximately by a factor of three over the range of speeds investigated. Lines show model predictions using parameters for the 1mm blade. (C) Average strain rate (symbols) measured as a function of applied stress during uniaxial tensile creep tests. A linear fit to the growing part of the curve (solid line) is extrapolated to zero strain rate to determine the yield stress $Y^* = 39$ MPa. Each type of symbol denotes a series of measurements performed on an individual ribbon sample. In each of these experiments, the imposed stress was incremented from zero in steps, and the strain was allowed to creep upwards at each step until it reached an approximately constant value. An average strain rate was estimated at each step by a linear fit to the data.

linearly above this threshold. A linear fit to the data above the plastic yield threshold in Fig. 2C gave a viscosity coefficient of $\Phi^* = 92 \pm 4$ GPa.s, and extrapolation of the curve to zero average strain rate provided an estimate of a yield stress of $Y^* = 39 \pm 1$ MPa. However, as shown in Fig. 2C, small but measurable plastic strain rates were also found below this estimate of the yield stress for applied stress values larger than 32 MPa. Finally, tensile stress relaxation experiments performed by rapidly ramping the strain imposed on a sample ribbon to a fixed value, and recording the reduction in stress that followed (see *SI Appendix*), yielded maximum rates of plastic stress relaxation that increased weakly up to 1.8 MPa/s at 1.6% imposed strain and then more sharply and approximately linearly to 8 MPa/s for 4.4% imposed strain, relaxing to stresses in the range 28–36 MPa, with evidence of yield taking place even at strains below 1%. In summary, the ratio $Y^*/E^* \lesssim 0.016$ measured under extensional deformation indicates that the ribbon is a stiff material with a relatively low (but poorly defined) yield threshold, while estimates of stress relaxation time range from below 1 s to approximately 40 s.

Physical interpretation. Figure 3 illustrates the mechanism that we propose to explain ribbon curling. The ribbon’s complex constitutive properties are idealised by treating it as an isotropic elastic/viscoplastic material with a yield stress Y^* and a stress-relaxation timescale t_p^* , such that the material be-

haves elastically over timescales much less than t_p^* but stresses in excess of Y^* relax over a timescale t_p^* via irreversible deformation of the material; in line with experimental observations, we allow ourselves some latitude in defining precise values of Y^* and t_p^* . We ignore friction between the ribbon and the blade, so that the ribbon bears a uniform load along its length and remains isothermal. We consider the motion of an element of ribbon as it passes onto, over and off the blade. In doing so, the curvature of the element (i) rises smoothly while the ribbon is off the blade, (ii) adopts the curvature of the blade while in contact with it, and then (iii)-(v) falls once off the blade (see Fig. 3, top), giving rise to stress distributions across the ribbon illustrated in Fig. 3 for low and high loads (cases A and B respectively). Although the ribbon adopts a steady shape, material elements experience a time-varying curvature as they pass over the blade. The off-blade curvature distributions (i, iii-v) are regulated by a balance between the ribbon’s bending resistance (which we assume is unaffected by any plastic deformation) and the imposed axial load. We assume that, as it passes over the blade, the ribbon element experiences a transverse strain gradient proportional to its instantaneous curvature, stretching the ribbon on its outer surface and compressing it (relatively) at its inner surface. Thus, upstream of the blade (i), the curvature-induced strain induces a transverse gradient of stress through an initial elastic response, which acts in addition to the axial loading on the ribbon. Where the stress exceeds Y^* , however, the ribbon

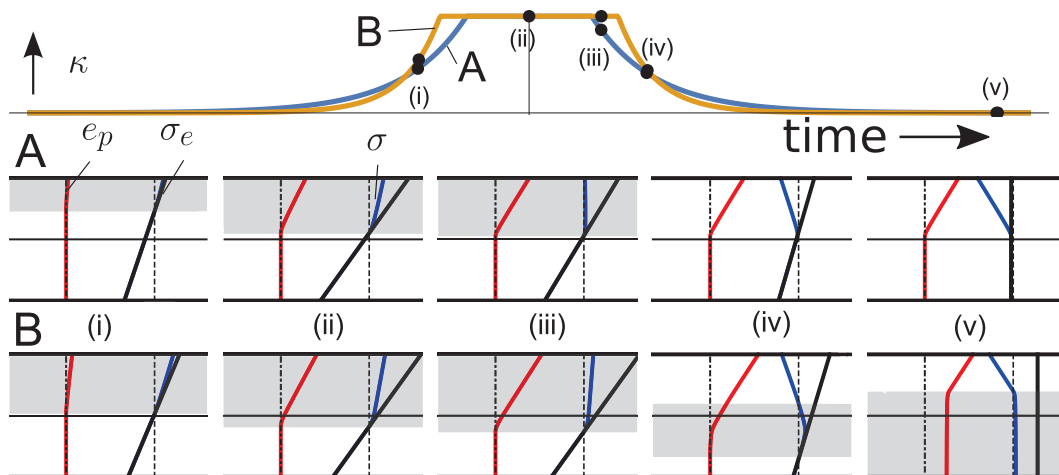


Fig. 3. Diagram illustrating the evolution of curvature, stress and plastic deformation of the ribbon for two parameter sets A and B, corresponding to the distinct regimes of behaviour identified in the model. The parameters used in the calculations are $t_p^* = 0.35$ s, $Y^* = 35$ Mpa, $E^* = 2.5$ GPa, $H^* = 100$ μ m and $R^* = 1$ mm, with applied loads $\Sigma^* = 10$ MPa in (A), and $\Sigma^* = 30$ MPa in (B). The top panel depicts the curvature κ of a material element of ribbon as a function of time as the element passes over the blade showing (i) pre-blade, (ii) on-blade and (iii-v) post-blade states. In these examples the ribbon comes into line contact with the blade, with its maximum curvature $1/R^*$ matching that of the blade. Increasing the axial load on the ribbon (going from (A) to (B)) reduces the lengthscale L_b^* over which the curvature decays off the blade and increases the width of the contact region. Panels A and B below depict profiles across the ribbon cross-section of the axial stress distribution σ (blue) and the axial plastic strain e_p (red). Black lines show σ_e , the total axial strain times Young's modulus; its transverse gradient is determined by the instantaneous curvature of the ribbon element. The shaded regions indicate the yielding domain, denoting regions where σ exceeds the yield stress (indicated with a dashed line). In (i), the increasing curvature raises σ above yield close to the outer surface of the ribbon; the material begins to relax, decreasing σ below σ_e and promoting a gradient in e_p . (ii) The stress integrated across the ribbon supports the constant imposed load, moving the yield surface towards the inner surface of the ribbon as the stress field relaxes. (iii) Just after leaving the blade, the yielded region is confined to the upper half of the ribbon under lower loads (A), but extends into the lower half of the ribbon under higher loads (B). (iv) The lowering curvature pivots the stress distribution around the ribbon midline: in (A) this lowers σ below the yield threshold, whereas in (B) the yielding region propagates further into the lower half of the ribbon. (v) As the ribbon element straightens, in (A) the final plastic strain is confined to the upper half of the ribbon whereas in (B) the entire ribbon cross-section has undergone yield, leading to net axial stretch. See Movies 1 and 2, which are published as supporting information on the PNAS web site.

starts to yield irreversibly (see (i, ii) of Fig. 3); initially, this takes place close to the ribbon's outer surface. As the stress in the yielded region relaxes, the yielded region widens in order that the ribbon element can support a constant net axial load. Passing off the blade, the stress in the yielded region relaxes towards Y^* , leaving the ribbon irreversibly elongated at its outer surface ((iii) in Fig. 3).

Passage of the element further off the blade leads to a reduction in curvature and hence in the transverse strain gradient. Thus, via an initial elastic response, there is a corresponding reduction in the transverse stress gradient; this may be visualized as counter-clockwise pivoting of the stress distribution about the ribbon's mid-line. If the yielded region remains confined to the upper half of the ribbon ((iv, v) in case A, Fig. 3), then no further yielding occurs. However if the yielded region penetrates into the lower half of the ribbon, pivoting of the stress lowers the stress near the outer wall but creates a new zone near the ribbon's mid-line where the stress exceeds Y^* , ((iv) in case B, Figure 3). This, in turn, induces a second phase of stress relaxation, involving widening of the central yielded region ((v) in case B, Fig. 3), and further irreversible elongation of the ribbon; this process is promoted by further curvature reduction as the ribbon element straightens out. Ultimately, the yielded region extends to the inner surface of the ribbon, reducing the gradient of irreversible strain. When unloaded, the curvature of the ribbon element is determined by the overall gradient of the net plastic strain; this gradient grows as the ribbon yields near its outer surface ((v) in case A, Fig. 3) but falls if there is additional yielding near the inner surface ((v) in case B, Fig. 3).

The minimal load required to induce a curl (Fig. 2A) can therefore be associated with the threshold required to induce

yield at the ribbon's outer surface; the increase of curvature with load is associated with thickening of this yielded region ((i)-(iii) in case A, Fig. 3); the reduction of curvature with load at higher load is due to the compensating yield near the inner surface ((iv, v) in case B, Fig. 3). The reduction of curvature with pulling speed (Fig. 2B) arises because the ribbon element has limited time in which to undergo stress relaxation while on the blade. Curling is maximized by driving the on-blade yield surface to the ribbon centreline (but not beyond), and by ensuring the ribbon moves slowly enough for the stress to relax fully before leaving the blade.

We can use experimentally measured parameters to estimate the load required to induce curling. We represent the load as an axial stress Σ^* and define the ratio of the ribbon's thickness H^* to the blade radius of curvature as $\epsilon \equiv H^*/R^*$, where $\epsilon \ll 1$. The ribbon will conform tightly to the blade if the bending length $L_b^* \equiv (E^*H^{*2}/\Sigma^*)^{1/2}$ (treating the ribbon as a loaded elastic beam) is small compared to R^* , i.e. $\Sigma^* \gg \epsilon^2 E^*$. Pre-blade, we require $\Sigma^* < Y^*$ (to avoid large-scale yielding) and the mean axial strain is $O(\Sigma^*/E^*)$. The additional strain at the outer ribbon surface induced by curving the ribbon over the blade is $O(\epsilon)$, inducing an elastic stress $O(\epsilon E^*)$. For yielding to take place, we therefore require Σ^* to lie in a window of width of order ϵE^* below Y^* . This explains why the threshold for curling is lower for sharper blades (Fig. 2A), but does not explain why the maximum load leading to curling falls for sharper blades. When the dimensionless *Curling number*,

$$C \equiv \frac{H^* E^*}{R^* Y^*}, \quad [1]$$

is small, curling takes place in a narrow window of loads with the ribbon conforming tightly to the blade; the maximum

equilibrium ribbon curvature can be expected to be comparable in magnitude to that of the blade. For larger \mathcal{C} , the curling window extends to low loads, encompassing (at the lowest loads) the case in which the ribbon bends gently over the blade. For sufficiently large \mathcal{C} , the resulting maximum equilibrium curvature is limited by the bending length of the ribbon to be of magnitude $1/(R^*\mathcal{C}) = Y^*/(H^*E^*)$ (i.e. $1/L_b^*$ with $E^*(H^*/L_b^*) = O(Y^*)$). Curling is reduced further if the on- or off-blade transit time falls beneath the stress-relaxation timescale, i.e. for $V^*t_p^* \gtrsim \min(R^*, L_b^*)$.

We now develop this qualitative explanation with a quantitative model, summarised briefly below and explained more fully in *Materials and Methods* and *SI Appendix*.

Model predictions. Model predictions are shown using lines in Fig. 2A. The model predicts that curling takes place for loads satisfying

$$\Sigma^* > Y^* - \frac{1}{2}\kappa_{\max}E^* \quad [2]$$

where the dimensionless curvature κ_{\max} is the minimum of the curvature of the blade H^*/R^* (which arises at higher loads, when the ribbon is in line contact with the blade, as in Fig. 3A) or the maximum beam curvature $\sqrt{48\Sigma^*/E^*}$ (this arises at lower loads, when the ribbon is bent through 90° and in point contact with the blade). Thus if $0 < \mathcal{C} < 2$, the curvature of the ribbon at the lower threshold for curling is set by the blade and the cut-off lies at $(1 - \frac{1}{2}\mathcal{C})Y^*$; for larger values of \mathcal{C} the cut-off is close to zero load (being $O(H^*Y^*/R^*)$) and the ribbon curvature at the onset of curling is regulated by bending effects.

The predicted ribbon curvature is composed of two curves, one rising with load and the second falling (Fig. 2A). On the rising curve, yield is confined to the upper half of the ribbon cross-section; on the falling curve, yield extends into the lower half of the cross-section. The threshold between the curves depends on geometric and material parameters, and the speed at which the ribbon passes over the blade. Choosing values of Y^* and t_p^* (within the range of experimentally determined values) to match measurements of peak curvature, the model underestimates the minimum load for the onset of curling (although it provides a qualitative explanation for this behaviour). Just as stress relaxation measurements reveal a range of yield stress values (see *SI Appendix*), it was not possible to identify a single parameter set appropriate for all four blades, reflecting limitations of the constitutive model. The maximum load for curling is closely related to the assumed yield stress (see (2)); experimental data show that the sharp blade induces yielding at a lower effective yield stress, which is reflected by choosing a lower value of Y^* . Curling is promoted by allowing for full stress relaxation while the ribbon is on the blade. As independent uniaxial tensile tests (*SI Appendix*, Fig. S1) show stress relaxation occurring more rapidly for larger strains, we adopt a smaller relaxation time for the experiments with sharper blades.

Lines on Fig. 2B show how the curvature is predicted to fall with increasing speed for a fixed load, using parameters for the 1mm blade. The rate of decay of curvature with speed is captured reasonably well, and the model confirms that greater curvature may generally be achieved at lower speeds (and higher loads) by allowing for complete stress relaxation in the upper half of the ribbon. Although not evident in the experimental data, the model predicts that this effect may be offset at very low speeds (to the left of the kink in predicted curves), where the yield surface penetrates the lower half of the ribbon: in this case the model suggests that slightly greater curvatures can be achieved under lower loads.

The model predicts net axial elongation (in addition to curling) that undergoes a transition from modest to steep increase with load at approximately the load required for maximum curvature (see Fig. 2A). Hence, net axial elongation is most significant along the falling part of the curvature-load curve. The experimental data confirm this prediction (*SI Appendix*, Fig. S2).

Discussion

Perhaps the most surprising feature of the experimental data reported here is the non-monotonic dependence of curvature on load, showing that the applied load must be carefully tuned in order to maximise permanent ribbon curvature when using a blade of given radius. The load applied to the ribbon serves multiple purposes: it wraps the ribbon over the blade, forcing it to curve; it elevates the axial stress in the ribbon towards the yield stress; and it regulates the pattern of plastic deformation across the cross-section of the ribbon. When the ribbon is curved, stretching of the ribbon at its outer surface may be sufficient to induce plastic deformation locally. This deformation is applied to a length of ribbon by running the ribbon over the blade, at a speed that is sufficiently slow for part of the ribbon’s cross-section to stretch irreversibly. If the stress relaxes while the ribbon is in a curved configuration, then straightening of the ribbon as it leaves the blade elevates the stress on the inner surface of the ribbon. If the load is sufficiently great, this can induce further plastic deformation, reducing the transverse strain gradients that lead to permanent curvature.

Experiments characterising the material properties of the ribbon under elongation demonstrate surprisingly complex constitutive properties, that we have not attempted to represent in full detail, choosing instead to work within the framework of a relatively simple (quasi-one-dimensional elastic-viscoplastic) constitutive model. Our semi-quantitative predictions are sufficient to provide the physical insight needed to rationalise ribbon curling, during which extensional, shear and viscous effects interact. Our model discounts frictional effects that may induce heating or surface deformations; these may contribute to curling in other circumstances.

The experimental protocol described here offers novel insights into material properties under shear of thin materials that are stiff but which yield at relatively low loads. The yield stress and relaxation time can be hard to define unambiguously for the polymer materials that often constitute ribbons, even in simple extensional tests. The curling number (1) and the dimensionless transit speed $V^*t_p^*/R^*$ are useful in characterising the range of loads over which curling arises and the tightness of the resulting curls.

Materials and Methods

Model description. A full description of the mathematical derivation and solution of the model can be found in *SI Appendix*. The following highlights the model’s key aspects.

To allow physical insight, our model seeks to capture the essential features of the experiment using a minimal number of parameters. We impose a strain field on a ribbon element as it moves from state to state and compute the resulting stress field. We calculate strain profiles by modeling the ribbon as an Euler–Bernoulli beam which is subject to an applied load and the constraint that it wraps around the blade for a portion of its length. This yields a curvature profile which is uniform on the blade and decays over a distance $L_b^* = (E^*H^{*2}/\Sigma^*)^{1/2}$ off it (Fig. 3, top). The ribbon element experiences a transverse strain gradient, induced by the imposed curvature, superimposed on a transversely uniform axial strain. As shown in *SI Appendix*, the ribbon is found to be in point contact with the blade at low loads (when $L_b^* \geq \sqrt{48}R^*$, where the maximum curvature is $\sqrt{48}/L_b^*$); it is in point contact with maximum curvature $1/R^*$ for slightly higher loads and in line contact with

maximum curvature $1/R^*$ for $L_b^* < R^* \sqrt{12(2 - \sqrt{2})}$. Given a ribbon speed V^* , this yields the curvature history $\kappa^*(t^*)$ of a material element. Examples are shown in **SI Appendix**, Figs S4–S6.

Given the imposed strain, we compute the stress by modelling the ribbon as a elastic/perfectly-viscoplastic (Bingham–Maxwell) material, parametrized by a stiffness E^* , a yield stress Y^* and a relaxation time t_p^* . We adopt a simplified representation for which the dominant stress and strain components in a ribbon element are purely axial and dependent on the transverse coordinate H^*h (with $-\frac{1}{2} < h < \frac{1}{2}$), responding parametrically to changes in the element’s curvature. As we do not use a fully three-dimensional formulation, we cannot expect estimates of the material parameters from unidirectional extensional deformations, which themselves show significant variability (Fig. 2C and **SI Appendix**), to transfer precisely to the more complex shear deformations associated with the curling experiment. Instead, we use the measured transit speed V^* , set $E^* = 2.5\text{GPa}$ (as measured) and adjust Y^* and t_p^* where they are used in the model within tightly defined ranges in order to fit the model to data. Having computed irreversible stretching of the ribbon element, its final curvature is computed by seeking its equilibrium configuration under zero load and moment.

To model plastic deformation, we non-dimensionalize lengths by the ribbon thickness H^* , stresses by the yield stress Y^* and time by $\pi R^*/2V^*$, the time taken to pass over the blade. The dimensionless compliance parameter $\eta = Y^*/E^*$ is assumed small. In terms of the transverse coordinate h , directed from the inner to the outer wall of an element of ribbon, the axial strain distribution is assumed to take the form $e(h, t) = \bar{e}(t) + \kappa(t)h$, with $\bar{e}(t)$ the element’s uniform stretch and $\kappa(t) = H^*\kappa^*$ the ribbon’s centreline curvature. With $\kappa(t)$ prescribed, $\bar{e}(t)$ adjusts to accommodate plastic deformations. Prior to any plastic deformation, $\bar{e}(t) = \eta\Sigma$ where $\Sigma = \Sigma^*/Y^*$ represents the net axial load on the ribbon. We assume a linear-elastic/plastic strain decomposition $e(h, t) = \eta\sigma(h, t) + e_p(h, t)$, with σ the axial stress and e_p the plastic strain. The Bingham–Maxwell elastic/perfectly-viscoplastic constitutive law [11] is

$$\frac{de}{dt} \equiv \eta \frac{d\sigma}{dt} + \frac{de_p}{dt} = \eta \frac{d\sigma}{dt} + \phi(\sigma - 1)H_v(\sigma - 1), \quad [3]$$

where $\phi = \pi R^*\eta/(2V^*t_p^*)$ is an extensibility parameter and H_v the Heaviside function. We adopt a quasi-one-dimensional formulation, disregarding shear stresses so that h appears as a parameter in (3); there is plastic deformation wherever $\sigma > 1$. The axial stress resultant balances the imposed load, giving

$$\int_{-1/2}^{1/2} \sigma(h, t)dh = \Sigma. \quad [4]$$

1. Timoshenko, S.P. et al. (1925) Analysis of bi-metal thermostats. *J. Opt. Soc. Am.* **11**, 233–255.
2. Nelson, M.R., Band, L.R., Dyson, R.J., et al. (2012) A biomechanical model of anther opening reveals the roles of dehydration and secondary thickening. *New Phytologist* **196**, 1030–1037.
3. Reyssat, E. & Mahadevan, L. (2009) Hygromorphs: from pine cones to biomimetic bilayers. *J. Roy. Soc. Interface* **6**, 951–957.
4. Reyssat, E. & Mahadevan, L. (2011) How wet paper curls. *EPL* **93**, 54001.
5. Moulia, B. & Fournier, M. (2009) The power and control of gravitropic movements in plants: a biomechanical and systems biology view. *J. Exp. Bot.* **60**, 461–486.

As shown in **SI Appendix**, this system can be reformulated as an integro-differential equation for e_p

$$\begin{aligned} \frac{de_p}{dt} &= \frac{\phi}{\eta} f[e_p]H(f[e_p]), \\ f[e_p] &= \int_{-1/2}^{1/2} e_p dh + \kappa h + \eta(\Sigma - 1) - e_p, \end{aligned} \quad [5]$$

which was solved numerically up until a time at which the stress had fully relaxed.

Once the load is removed from the ribbon, each element relaxes to form a coil with the ribbon’s centreline having a constant equilibrium curvature κ_c and average strain $e_c = \bar{e}_c + \kappa_c h$. The blade-induced residual strain $e_p(h)$ means the stress in this state is $\sigma(h) = (e_c(h) - e_p(h))/\eta$, and we enforce force and moment balance under zero applied load and couple,

$$\int_{-1/2}^{1/2} \sigma dh = 0, \text{ and } \int_{-1/2}^{1/2} h\sigma dh = 0, \quad [6]$$

to give \bar{e}_c and κ_c . Solutions of the numerical model are shown in Figs 3 and S7–S10.

In addition, we show in **SI Appendix** how (5) can be simplified in the limit of rapid stress relaxation to deduce an analytic approximation for the rising part of the curve relating equilibrium curvature κ_c and imposed load Σ , namely

$$\frac{\kappa_c}{\kappa_{\max}} = 1 + 2 \left(\frac{2\eta(1 - \Sigma)}{\kappa_{\max}} \right)^{3/2} - 3 \left(\frac{2\eta(1 - \Sigma)}{\kappa_{\max}} \right) \quad [7]$$

where $\kappa_{\max} = \min(\epsilon, \sqrt{48\Sigma\eta})$, for $\frac{1}{8}\kappa_{\max} < \eta(1 - \Sigma) < \frac{1}{2}\kappa_{\max}$ (see **SI Appendix**, Fig. S11). In this limit the ribbon is predicted to be entirely in point contact with the blade for $\mathcal{C} > 8$, with maximum $\kappa^* = 4/\mathcal{C}R^*$, whereas for $\mathcal{C} < 8$ the maximum predicted curvature is $\kappa^* = 2/R^*$ with the ribbon in line contact with the blade. In practice, finite relaxation times reduce measured curvatures below the upper bound predicted by this approximation.

ACKNOWLEDGMENTS. C.P. was supported by an Addison-Wheeler fellowship. We thank H. Cass and A. Crowe for preliminary experiments, E. Häner for help with image analysis, and D. Pihler-Puzović for measurements of Young’s modulus. B.C. thanks A. M. Klales, P. Hine for preliminary experiments and V. Vitelli, V. N. Manoharan, and L. Mahadevan for preliminary discussions. We are grateful to a referee for valuable suggestions relating to our numerical solution scheme.

6. Chou, M.-H., Shen, W.-C., Wang, Y.-P. et al. (2014) Curling edges: A problem that has plagued scrolls for millennia. *Phys. Rev. Lett.* **112**, 034302.
7. Štok, Halilović (2009) Analytic solutions in elasto-plastic bending of beams with rectangular cross section. *Appl. Math. Mod.* **33**, 1749–1760.
8. Kebabdz, E., Guest, S.D. & Pellegrino, S. Bistable prestressed shell structures. *Int. J. Solids Struc.* **41**, 2801–2820.
9. Balmforth, N.J. & Hewitt, I.J. (2013) Viscoplastic sheets and threads. *J. Non-Newton. Fluid Mech.* **193**, 28–42.
10. Young, R.J. & Lovell, P.A. (2011) Introduction to polymers (3rd ed.), CRC Press.
11. Lubliner, J. (2008) Plasticity theory. Dover. Mineola, New York.

Ribbon curling - Supplement

Chris Prior ^{*}, Julien Moussou [†], Buddhapriya Chakrabarti ^{*}, Oliver E. Jensen [‡] and Anne Juel [‡]

^{*}University of Durham, Durham, UK, [†]University of Manchester, Manchester, UK, and [‡]Ecole Normale Supérieure, Paris, France

Submitted to Proceedings of the National Academy of Sciences of the United States of America

In this document we follow the convention of the main paper that all dimensional quantities will be labelled with * superscript and non-dimensionalised variables will be unmarked.

Experimental Materials and Methods

Experiments were performed with polyvinyl chloride (PVC) transparency films of a thickness of $H^* = 100 \pm 3 \mu\text{m}$, which were cut into ribbons of length of $260 \pm 0.3 \text{ mm}$ or $292 \pm 0.3 \text{ mm}$, and width $W^* = 10 \pm 0.3 \text{ mm}$ (West Films, Write-On FLM510200 and FLM510210). One end of the ribbon was bonded with double-sided tape to a rotating cylinder (of radius $12.60 \pm 0.05 \text{ mm}$ diameter), which was rotated uniformly about its horizontal axis. The rotation of the cylinder was driven by a d.c. motor (Maxtor) connected to a 100:1 gearbox, resulting in the winding of the ribbon around the cylinder at constant linear pulling speeds of $0.9 \text{ mm/s} < V^* < 25 \text{ mm/s}$. The other end of the ribbon was attached to a clamp, which could be loaded with weights, so that the ribbon was pulled vertically downward due to gravitational acceleration by masses in the range $50 \text{ g} \leq m^* \leq 2500 \text{ g}$. A horizontal blade, which was machined out of aluminium and wider than the ribbon, was positioned at a distance of 45 mm away from the axis of the cylinder, so that the weight-loaded ribbon was forced to bend sharply over the surface of the blade from an approximately horizontal to a vertical configuration. The blades had radii of curvature $R^* = 1.04 \pm 0.07 \text{ mm}$, $1.51 \pm 0.10 \text{ mm}$, $2.03 \pm 0.06 \text{ mm}$ except for the sharp blade which had $R^* < 0.1 \text{ mm}$.

After the ribbon had been pulled over the blade to form at least one curl, it was carefully removed from the cylinder, cut to size and transferred to a back-lit translucent Perspex plate for visualisation. The curled ribbon was positioned on its edge and allowed to relax between one and five minutes before a photograph was taken with a digital camera (Nikon D80), as shown in the left-hand image of Fig. 1C in the main paper. The images were processed in MATLAB by firstly detecting the outer edge of the circular ribbon profile using the “Canny” method, and secondly applying the Hough transform method to fit a circle to the measured outline, whose inverse radius gave the curvature of the ribbon (see Fig. 1C). This secondary fitting procedure enabled the measurement of the radius of curvature with sub-pixel resolution, resulting in errors on the radius of approximately 0.1 mm. The experimental procedure, which included the manipulation of the curled ribbon, meant that the measurement of radii of curvature became increasingly delicate the looser the curls. Hence, we were only able to measure curvatures reliably down to values of approximately 0.30 cm^{-1} . A single mastercurve of ribbon curvature as a function of load $\Sigma^* = m^*g/(H^*W^*)$ was obtained when using three ribbon widths $W^* = 10 \text{ mm}$, 15 mm and 20 mm .

The results of stress relaxation experiments on ribbons under uniaxial tension are shown in Fig. S1. Experiments were performed on 9 identical PVC ribbons (with length, width and thickness of 190 mm, 20 mm and $80 \mu\text{m}$, respectively). In each experiment, the ribbon was extended to a set value of strain, at a constant rate of $4.9 \times 10^{-3} \text{ s}^{-1}$, before it was left to relax. The plot of measured stress as a function of imposed strain (Fig. S1A) resembles a constitutive curve, albeit measured at high strain rates. Stress increases linearly

for small strain before reaching a plateau, which is associated with visco-plastic yield of the material. Reduction in stress is observed at all set values of strain, indicating that relaxation occurs on time scales longer than the pulling timescale in all cases. The maximum value of the pulling timescale is 9 s for a strain $e = 0.045$. The associated variation of stress with time is shown in Fig. S1B over a period of 180 s. The maximum rate of stress relaxation increases monotonically with applied strain. However, the results shown in Fig. S1 also indicate that once the ribbon yields, the stress relaxes to a range of values $32 \leq \Sigma^* \leq 39 \text{ MPa}$, where the upper bound is the measured value of yield stress (Fig. 2C in the main paper). These results demonstrate that the material is associated with a range of yield stress values, and that its viscoplastic time scale depends on strain. This complex behaviour is linked to the proximity of the glass transition (which occurs for PVC at a temperature $T_g \simeq 80^\circ\text{C}$ that decreases upon addition of plasticisers) to the laboratory temperature of $21 \pm 1^\circ\text{C}$, resulting in load dependent stress-relaxation behaviour shown in Fig. S1 [1, 2].

The extension of the ribbon relative to its initial length, or net strain, was measured after curling the ribbon over the sharp and $R^* = 1 \text{ mm}$ blades at $V^* = 4.9 \text{ mm/s}$. Lines were drawn across the ribbon with a thin-tipped permanent marker prior to experimentation in order to delimit a 120 mm long segment of ribbon. The measurement segment was photographed with a high resolution camera before and after curling, by pressing the ribbon down onto a flat surface with a metal ruler. The measurement error on the length of the segment using this technique was approximately $\pm 0.08 \text{ mm}$, yielding measurement errors on the net strain of approximately $\pm 0.1\%$. The experimental results shown in Fig. S2A indicate a steep increase in total ribbon strain beyond the load where the maximum curvature was reached (see Fig. 2A in the main paper). For this range of loads, the initially transparent ribbon became translucent during curling, indicating a significant change in internal structure. Average strain predictions in the model shown in Fig. S2B are in qualitative agreement with the experimental results, although the experimental strain values are considerably larger than the theoretical values (by approximately a factor of 4). Tensile tests were performed after curling on the sharp and 1mm blades. Curled ribbons with curvature below the maximum value for each blade exhibited a very small decrease in Young’s modulus with a value approximately 2% below the value of $E^* = 2.5 \pm 0.4 \text{ GPa}$ measured for straight ribbons. However, beyond the maximum curvature, where the net extension of the ribbon was significant,

Reserved for Publication Footnotes

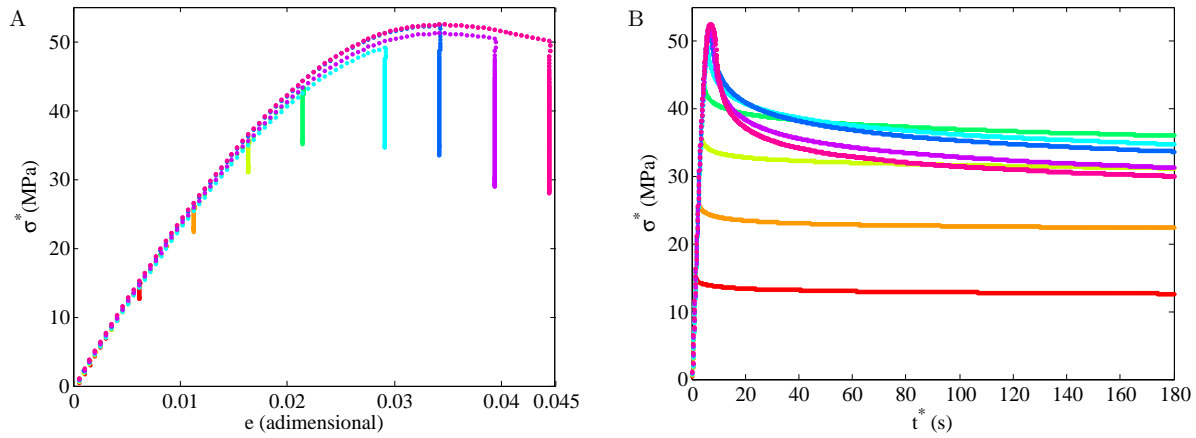


Fig. S1. Results from stress relaxation experiments, where a ribbon is extended uniaxially at constant rate to a set value of strain, and then left to relax. The different colours refer to experiments at different values of the set strain, which were performed on identical PVC ribbons. (A) Variation of stress with strain; (B) Variation of stress with time.

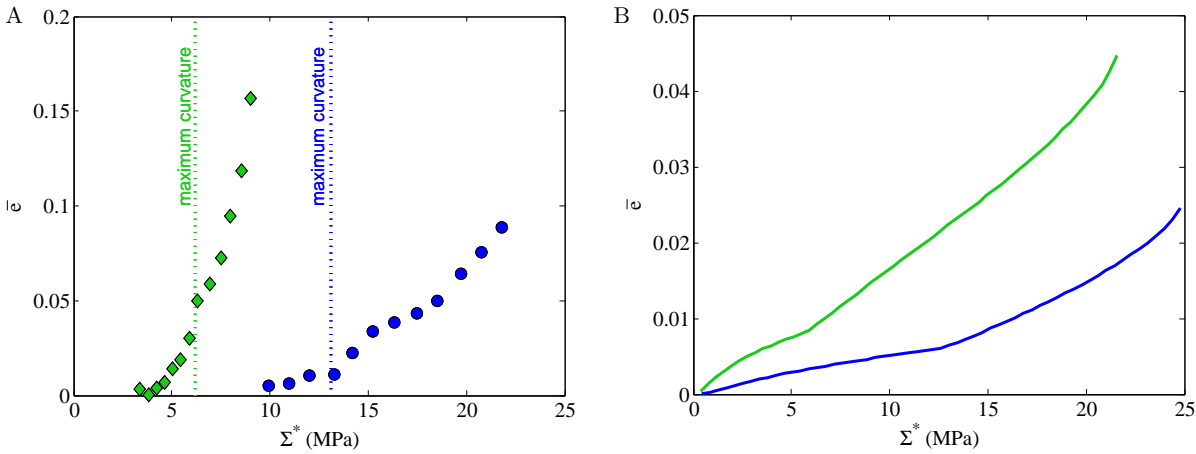


Fig. S2. Net strain as a function of applied load for $V^* = 4.9$ mm/s over the sharp blade (green) and the $R^* = 1$ mm blade (blue). (A) Experimental measurements. (B) Theoretical predictions of average net strain using the same parameters as in Fig. 2A in the main paper.

the Young’s modulus was found to decrease by up to 14% for curls formed with the sharp blade. Hence, the softening of the ribbon beyond the load yielding maximum curvature may contribute to the large values of total strain obtained experimentally in Fig. S2A. In addition, the contribution from shear effects neglected in the model (i.e. strain gradients above the gradient given by the curvature of the ribbon centreline), which increases with the curvature of the blade, may also add to the discrepancy in total strain values between experiments and numerical results.

Model derivation

In the following we describe how bending effects are used to determine the strain in the ribbon and then explain how the resulting stress field induces yielding. Numerical solutions of the model are supplemented with an asymptotic approximation in the limit of rapid stress relaxation.

Deriving the strain. We first represent the ribbon as an Euler–Bernoulli beam [3], defined by its unit tangent vector \mathbf{d}_1 and

unit normal vector \mathbf{d}_2 , with

$$\mathbf{d}_1 = (\cos \theta(s^*), \sin \theta(s^*)), \quad \mathbf{d}_2 = (-\sin \theta(s^*), \cos \theta(s^*)), \quad [1]$$

where $\theta(s^*)$ is the angle made with the x -axis, $\theta(0) = 0$, and arclength s^* is measured from the centre of contact with the blade and the ribbon (Fig. S3A). The ribbon has an associated cross-sectional force $\mathbf{n}^* = n_1^* \mathbf{d}_1 + n_2^* \mathbf{d}_2$ and couple $\mathbf{m}^* = D^* \theta_{s^*} \mathbf{d}_1 \times \mathbf{d}_2$; the subscript s^* denotes differentiation with respect to arclength and D^* is a material parameter representing the coefficient of bending of the ribbon. As the ribbon has a rectangular cross section, $D^* = E^* H^{*3} W^* / 12$ [4], with E^* the Young’s modulus, H^* the ribbon thickness and W^* its width. The balance equations for the ribbon are [3]

$$\mathbf{n}_{s^*}^* + \mathbf{f}^* = \mathbf{0}, \quad \mathbf{m}_{s^*}^* + \mathbf{d}_1 \times \mathbf{n}^* = \mathbf{0}, \quad \mathbf{f}^* = f_1^* \mathbf{d}_1 + f_2^* \mathbf{d}_2, \quad [2]$$

with \mathbf{f}^* a force density acting along the length of the ribbon.

The ribbon is pulled over a circular blade by a net axial force of magnitude $N^* = H^* W^* \Sigma^*$, directed at an angle θ_e with respect to the x -axis (Fig. S3A). For the sake of simplicity we treat the ribbon as infinitely long, assuming that $\theta \rightarrow \pm \theta_e$ as $s^* \rightarrow \pm \infty$. We assume that the ribbon wraps

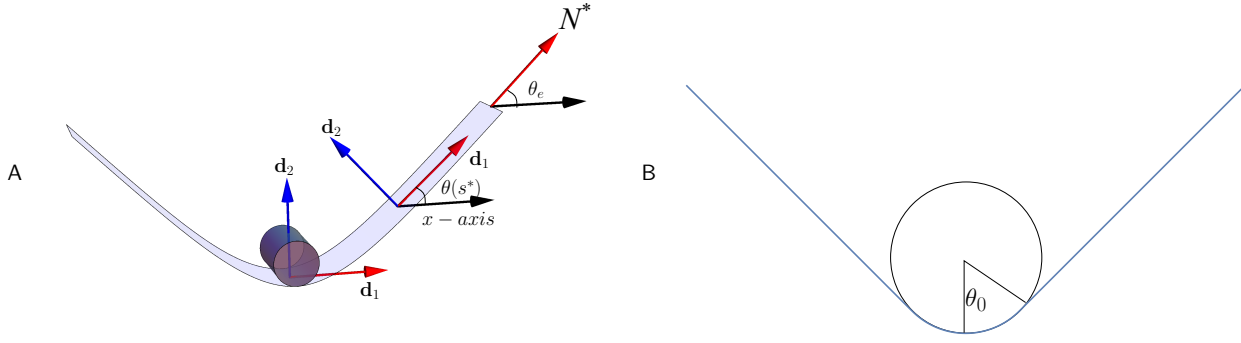


Fig. S3. (A) Schematic diagram of the beam model. The tangent \mathbf{d}_1 and normal \mathbf{d}_2 to the ribbon's axis are shown. Also shown is the angle $\theta(s^*)$ which defines these vectors and the angle θ_e between \mathbf{d}_1 and the x -axis, which is the angle indicating the direction of the applied load N^* . (B) Schematic diagram depicting the angle θ_0 at which the beam loses contact with the blade.

around the blade adopting its curvature κ_b^* for a sub-domain $\theta \in [-\theta_0, \theta_0] \subset [-\theta_e, \theta_e]$. For low applied loads it will transpire that the domain $[-\theta_0, \theta_0]$ reduces to a single point of contact.

By treating the ribbon as an Euler–Benoulli beam we do not allow the possibility of shearing deformations (off-diagonal components of the strain tensor). More advanced formulations, such as the Timoshenko beam [5], allow for such effects. However, unlike the Euler–Benoulli beam, they are not generally integrable systems [6]. We have chosen to use the simpler shear-free system in order to obtain closed-form expressions for the ribbon's kinematics; this greatly simplifies the plastic modelling in the proceeding section and is ultimately justified by the quality of the full model predictions. For the same reasons we ignore the effects of friction in what follows.

It is convenient to introduce the following non-dimensional quantities,

$$\begin{aligned} \mathbf{n}^* &= Y^* H^{*2} \mathbf{n}, & \mathbf{f}^* &= Y^* H^* \mathbf{f}, & s^* &= s H^*, \\ \kappa^* &= \kappa / H^*, & N^* &= Y^* H^{*2} N, & D^* &= Y^* H^{*4} D, \end{aligned} \quad [3]$$

with Y^* is the ribbon's yield stress. In component form, (2) becomes

$$\begin{aligned} n_{1s} - \theta_s n_2 + f_1 &= 0, \\ n_{2s} + \theta_s n_1 + f_2 &= 0, \\ D\theta_{ss} + n_2 &= 0. \end{aligned} \quad [4]$$

Neglecting gravity, a body force \mathbf{f} is only present where there is contact between the ribbon and the blade. We construct solutions in two parts: one for $|s| < s_0$, say, in which the ribbon has uniform curvature $\theta_s = \kappa_b \equiv H^*/R^*$ (where R^* is the blade radius) and a non-zero contact force f_2 (*on-blade*); the other for $|s| > s_0$ in which the free ribbon's curvature decays from κ_b at the point where it leaves the blade to 0 far from the blade (*off-blade*). We use matching conditions to create a closed system. The solution is symmetric about $\theta = 0$, as suggested by the symmetry of the boundary conditions under the transformation $s \rightarrow -s$.

On-blade, with $\theta_s = \kappa_b$ and $\theta_{ss} = 0$, (4) implies that n_2 vanishes so that the system reduces to

$$n_{1s} + f_1 = 0, \quad \kappa_b n_1 + f_2 = 0. \quad [5]$$

In the absence of any tangential forces (*e.g.* friction), $f_1 = 0$, n_1 is constant and $f_2 = -n_1/\kappa_b$. To assign a value to n_1 we need to consider the matching conditions, requiring continuity of θ_s across $s = s_0$ where $\theta = \theta_0$ (Fig. S3B).

Off-blade, where $\mathbf{f} = \mathbf{0}$, (2) shows that \mathbf{n} will be constant. If we consider the section of ribbon in $s > 0$, noting that an axial load $N\mathbf{d}_1$ is applied where $\theta \rightarrow \theta_e$ for $s \rightarrow \infty$, it follows

that $\mathbf{n} = N(\cos \theta_e, \sin \theta_e)$. This boundary condition and the first two equations of (4) are satisfied if

$$n_1 = N \cos(\theta_e - \theta), \quad n_2 = N \sin(\theta_e - \theta). \quad [6]$$

The transformation $s \rightarrow -s$ and $\theta \rightarrow -\theta$ gives $n_1 \rightarrow n_1$ and $n_2 \rightarrow -n_2$ as expected. If we assume both θ_s and n_1 are continuous where the ribbon leaves the blade, *i.e.* across $s \in [s_0^-, s_0^+]$, then we can integrate the first equation of (4) to obtain

$$[n_1]_{s_0^-}^{s_0^+} = 0 \Rightarrow n_1(s_0) = N \cos(\theta_e - \theta_0). \quad [7]$$

This value will be the same for both branches of the solution. However there must be a discontinuity in the value of n_2 across s_0 , from zero on the blade to a non-zero value off it, necessitating a Dirac δ -function contribution to the contact force of the form

$$f_2 = -\kappa_b n_1 H_v(s_0 - s) + F \delta(s - s_0), \quad [8]$$

with H_v the Heaviside function. Integrating equation 2 of (4) gives

$$[n_2]_{s_0^-}^{s_0^+} + F = 0 \Rightarrow F = -N \sin(\theta_e - \theta_0). \quad [9]$$

The value of F reverses for the negative s branch of the solution. One can integrate \mathbf{f} over the on-blade domain to find the net applied force on the blade from one half of the ribbon to be $N \cos \theta_e$.

To compute the off-blade shape of the ribbon, the third equation of (4) reduces to

$$D\theta_{ss} - N \sin(\theta - \theta_e) = 0.$$

Rescaling s with $s = \hat{s} \sqrt{D/N}$, multiplying by θ_s , and integrating gives

$$\frac{1}{2} (\theta_s)^2 + \cos(\theta - \theta_e) = C_1. \quad [10]$$

The condition $\theta_s \rightarrow 0$ as $\theta \rightarrow \theta_e$ gives $C_1 = 1$, yielding a non-linear pair of ODEs for θ_s :

$$\theta_s = \pm \sqrt{2(1 - \cos(\theta - \theta_e))}.$$

For $\hat{s} > 0$, θ is increasing so we choose the positive root. We can then write

$$\hat{s} - \hat{s}_0 = \frac{1}{\sqrt{2}} \int_{\theta_0}^{\theta} \frac{d\theta}{\sqrt{1 - \cos(\theta - \theta_e)}}. \quad [11]$$

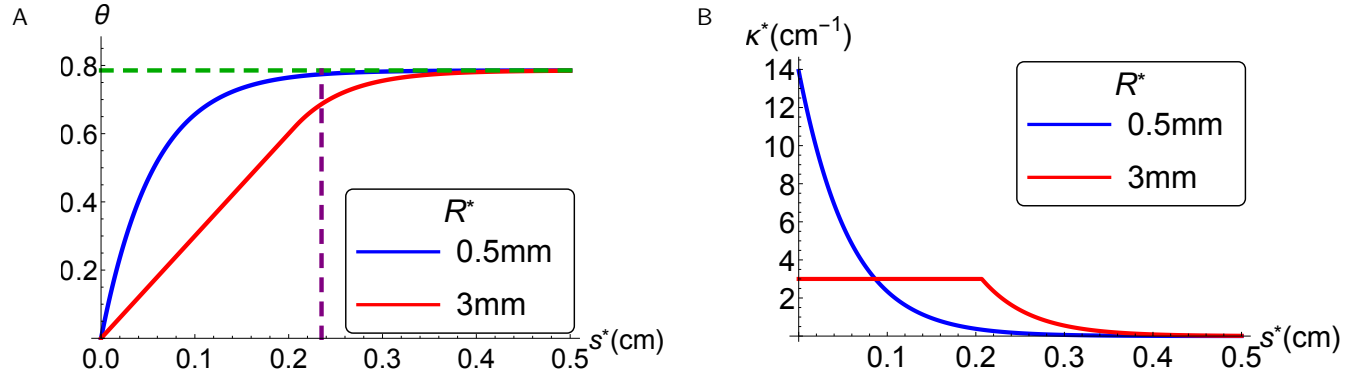


Fig. S4. (A) Representative plots of $\theta(s^*)$ in the case where there is point contact ($R^* = 0.5$ mm) and line contact ($R^* = 3$ mm). The angle increases quickly before asymptoting to $\pi/4$. For $R^* = 3$ mm the vertical dotted line indicates the transition between line and point contact between the ribbon and the blade. (B) Curvature $\kappa^*(s^*)$ for the same parameters used in (A). The curvature is constant on-blade ($R^* = 3$ mm).

It follows that

$$\hat{s}(\theta) - \hat{s}_0 = \log\left(\cot\left(\frac{\theta_e - \theta}{4}\right)\right) - \log\left(\cot\left(\frac{\theta_e - \theta_0}{4}\right)\right). \quad [12]$$

Writing $L_0 = \log\left(\cot\left(\frac{\theta_e - \theta_0}{4}\right)\right)$ yields

$$\theta(\hat{s}, \theta_0) = \theta_e - 4 \operatorname{arccot}\left(e^{\hat{s} - \hat{s}_0 + L_0}\right). \quad [13]$$

From this we obtain the curvature distribution $\kappa = \hat{\kappa}/\sqrt{D/N}$ where

$$\hat{\kappa}(\hat{s}, \theta_0) \equiv \theta_{\hat{s}}(\hat{s}, \theta_0) = 2 \operatorname{sech}(\hat{s} - \hat{s}_0(\theta_0) + L_0(\theta_0)). \quad [14]$$

It remains to compute the value of θ_0 . Enforcing the requirement that $\theta_{\hat{s}}(\hat{s}_0) = \hat{\kappa}_b$, where $\hat{\kappa}_b = \kappa_b \sqrt{D/N}$, gives

$$L_0 = \log\left(\frac{2 \pm \sqrt{4 - \hat{\kappa}_b^2}}{\hat{\kappa}_b}\right),$$

and hence

$$\theta_0 = \theta_e - \operatorname{arccot}\left(\frac{2 \pm \sqrt{4 - \hat{\kappa}_b^2}}{\hat{\kappa}_b}\right). \quad [15]$$

Unscaling the arclength variable ($\hat{s} = s/\sqrt{D/N}$) gives

$$\theta_0 = \theta_e - \operatorname{arccot}\left(\frac{2 \pm \sqrt{4 - \frac{D}{N} \kappa_b^2}}{\sqrt{D/N} \kappa_b}\right). \quad [16]$$

The location of the contact point is regulated by the dimensionless parameter $\sqrt{D/N} \kappa_b \equiv L_b^*/(12R^*)$ (in terms of the bending length $L_b^* = (E^* H^{*2}/\Sigma^{*2})^{1/2}$ defined in the main paper). Thus in the limit $N \gg \kappa_b^2 D$ the ribbon wraps tightly around the blade ($\theta_0 \rightarrow \theta_e$).

We summarise the predictions of the bending calculation for which the ribbon is in line contact with the blade in terms of the parameters Σ and $\eta = Y^*/E^*$ through the relation $N/D = 12\eta\Sigma$, parameters appearing in the plastic relaxation

calculation below:

$$\theta(s, \theta_e, \kappa_b, \Sigma, \eta) = \theta_e - 2 \operatorname{arccot}\left(e^{(s-s_0)\sqrt{12\Sigma\eta} + L_0}\right), \quad [17]$$

$$\kappa(s, \kappa_b, \Sigma, \eta) = \sqrt{48\Sigma\eta} \operatorname{sech}\left((s-s_0)\sqrt{12\Sigma\eta} + L_0\right), \quad [18]$$

$$\theta_0(\kappa_b, \Sigma, \eta) = \theta_e - \operatorname{arccot}\left(\frac{2 + \sqrt{4 - 12\Sigma\eta\kappa_b^2}}{\sqrt{12\Sigma\eta\kappa_b}}\right), \quad [19]$$

$$s_0(\kappa_b, \Sigma, \eta) = \frac{\theta_0(\kappa_b, \Sigma, \eta)}{\kappa_b}, \quad [20]$$

$$L_0(\kappa_b, \Sigma, \eta) = \sqrt{12\Sigma\eta} \log\left(\frac{2 + \sqrt{4 - 12\Sigma\eta\kappa_b^2}}{\sqrt{12\Sigma\eta\kappa_b}}\right). \quad [21]$$

For low net loads ($\Sigma \in [0, \Sigma_b]$, say), (19) will not yield real solutions for θ_0 , implying that the ribbon makes point contact with the blade at $\theta = s = 0$. Setting $\theta_0 = 0$ in (19) yields the load at which the ribbon changes from point to line contact

$$\Sigma_b = \frac{\kappa_b^2}{\eta(24 - 24 \cos \theta_e)}. \quad [22]$$

This load increases with κ_b and decreases with θ_e , reflecting the fact that at lower angles it becomes harder to pull the ribbon into line contact with the blade. For $\Sigma < \Sigma_b$, the ribbon's peak curvature can be found by inserting $\theta_0 = s_0 = s = 0$ in (18), giving

$$\kappa_{\max} = \min(\kappa_b, \sqrt{48\Sigma\eta} \sin(2\theta_e)). \quad [23]$$

In particular if $\theta_e = \pi/4$, as in most of our experiments, we have $\kappa_{\max} = \sqrt{48\Sigma\eta}$ provided $\Sigma < \kappa_b^2/48\eta$, so that the ribbon's peak curvature falls below the blade curvature at very low loads.

Predicted ribbon shapes. Fig. S4A shows representative plots of $\theta(s^*)$ using the experimentally determined values for H^* , W^* and E^* detailed in *Experimental Materials and Methods*, and a load $\Sigma^* = 5$ Mpa. The plots for $R^* = 0.5$ mm depict a case for which the ribbon has only point contact whilst for $R^* = 3$ mm there is line contact. Fig. S5 shows $\kappa^*(s^*)$ for the experimental blade radii and a representative set of loads. As the curvature of the blade is increased the width of ribbon-blade contact region decreases. For the sharp blade there is point contact for all loads.

Fig. S6 shows shapes of the ribbon centreline \mathbf{r} , obtained by solving $d\mathbf{r}/ds = (\cos \theta(s), \sin \theta(s))$ subject to $\mathbf{r}(0) = (0, 0)$ and

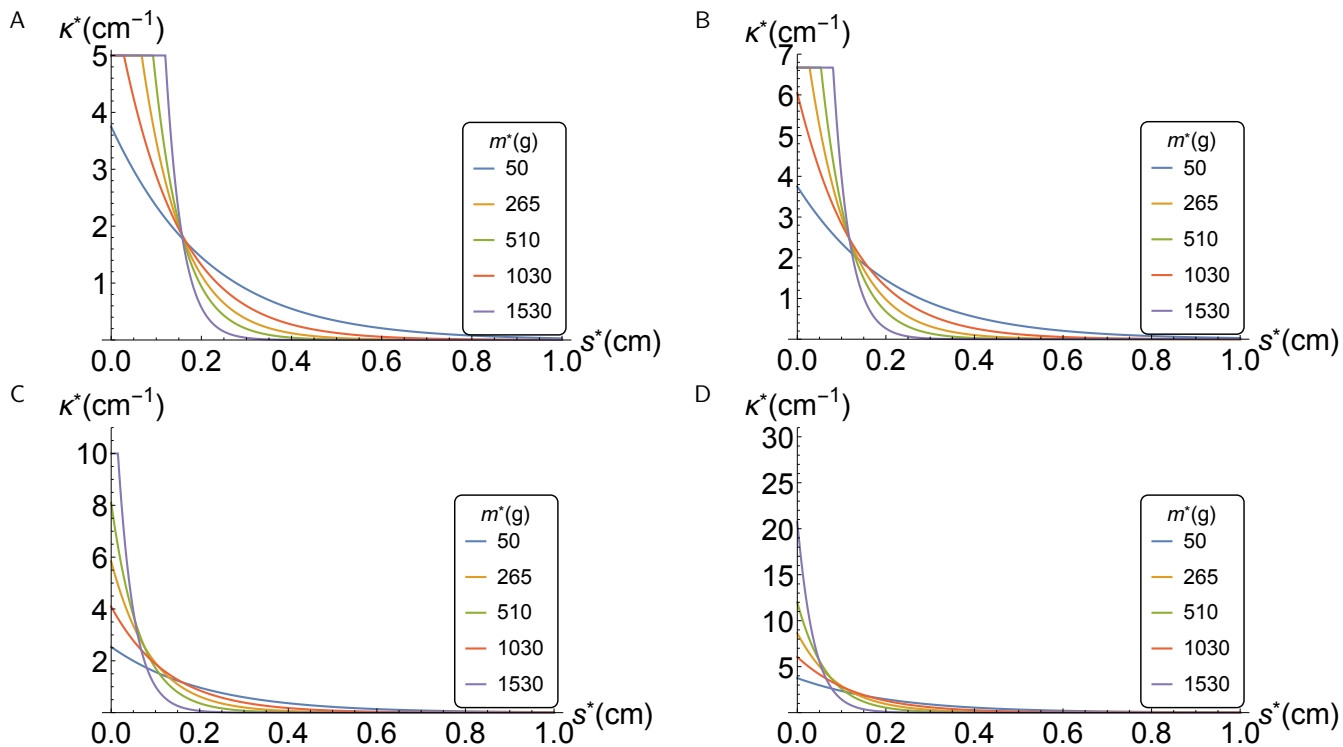


Fig. S5. Plots of curvature as a function of arclength, using the experimental parameters. The plots (A)-(D) are for the $R^* = 2$ mm, 1.5 mm, 1 mm and sharp blades. On each plot the curves are calculated for the loads used in Fig. 1B in the main paper. The ribbon is pulled at an angle of $\theta = \pi/4$ except for the $R^* = 1$ mm blade, where the angle is $\theta = 2/3(\pi/4)$ consistently with the experiments shown in Fig. 1B. The rate of decay off-blade increases with load. For a given curvature, an increase in load leads to an increase in the width of line contact between the ribbon and the blade.

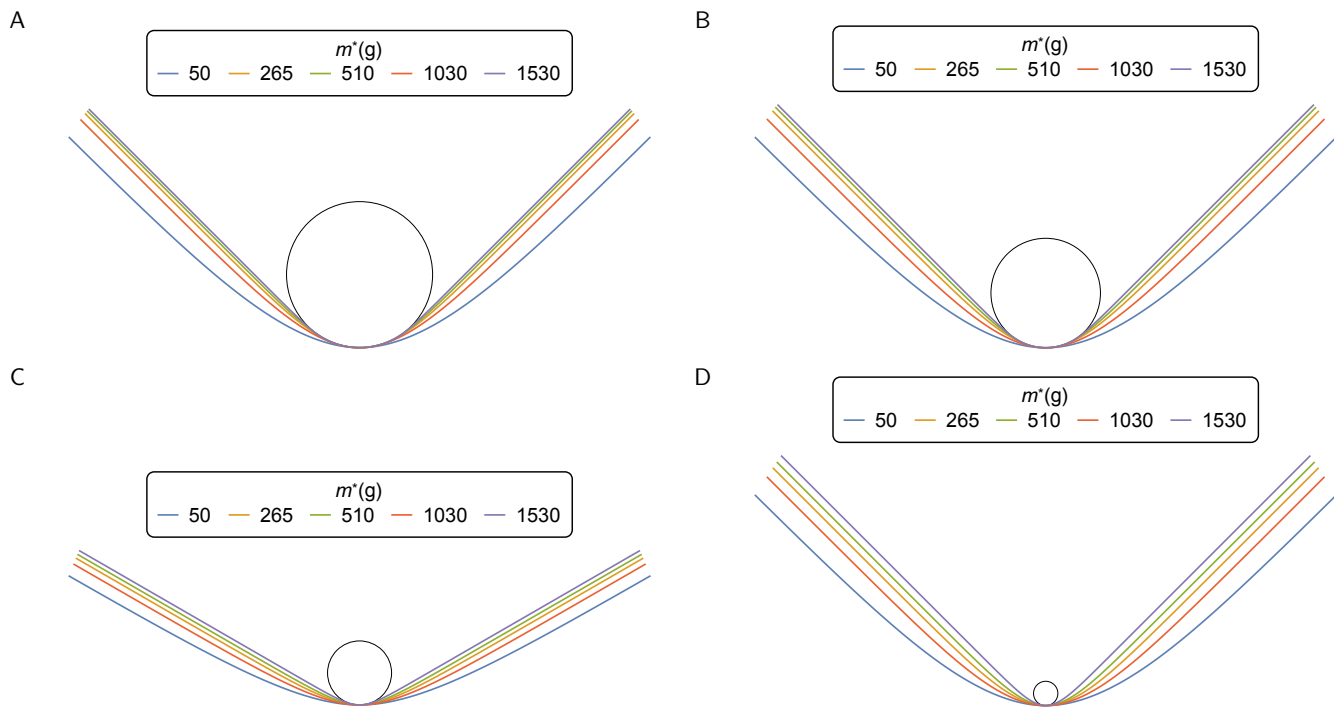


Fig. S6. Plots of the ribbon shape using the experimental parameters. Plots (A)-(D) are for the $R^* = 2$ mm, 1.5 mm, 1 mm and sharp blades. On each plot the curves are calculated for the loads used in Fig. 1B in the main paper. The ribbon is pulled at an angle of $\theta = \pi/4$ except for the $R^* = 1$ mm blade, where the angle is $\theta = 2/3(\pi/4)$ consistently with the experiments shown in Fig. 1B. The circles represent the blades and are drawn to scale. For the larger blades, all the configurations except the 50g case bunch together, similar to the observed configurations of Fig. 1B.

utilising the symmetry of the problem. The figures are a good match to the experimentally observed configurations shown in

Fig. 1B in the main paper. As before, the ribbon is unable to adopt the shape of the sharp blade, even at the highest load.

Modelling plastic deformation. We now consider the passage of an element of the ribbon over the blade, parametrising its position with respect to the blade by a time-like parameter t^* , taking $t^* = 0$ at $s^* = 0$. We assume the element is subject to a strain distribution

$$e(h^*, t^*) = \bar{e}(t^*) + \kappa^*(s^*(t^*))h^*. \quad [24]$$

The curvature κ^* of the element's centerline (determined by the results of the previous section) creates a strain gradient across the ribbon's cross section; $h^* \in [-H^*/2, H^*/2]$ measures distance across the cross section and \bar{e} is the uniform stretch. This prescription of $\kappa^*(t^*)$ restricts the permissible change in geometry of the ribbon's centreline to stretching deformations. We neglect feed-back between the plastic relaxation of the system and the curvature distribution in order to keep the problem relatively tractable; this assumption is supported by the observation in *Experimental Materials and Methods* that the Young's modulus does not change appreciably when the ribbon curls. Once again we distinguish cases in which the ribbon is in point or line contact with the blade.

To include plastic effects we assume a linear strain decomposition $e = (\sigma^*/E^*) + e_p$, with $\sigma^*(h^*, t^*)$ the axial stress and $e_p(h^*, t^*)$ the plastic strain. We assume a viscoplastic constitutive law

$$e_{t^*} = \frac{\sigma^*_{t^*}}{E^*} + e_{p,t^*} \equiv \frac{\sigma^*_{t^*}}{E^*} + \phi^*(\sigma^* - Y^*)H_v(\sigma^* - Y^*). \quad [25]$$

Here ϕ^* is the inverse viscosity, so that the material's relaxation time is $t_p^* = 1/(E^*\phi^*)$. Plastic deformation takes place for $\sigma^* > Y^*$. This corresponds to the Bingham-Maxwell elastic/perfectly-viscoplastic model [7]. An axial stress balance implies

$$\int_{-H^*/2}^{H^*/2} \sigma(h^*, t^*) dh^* = H^*\Sigma^*. \quad [26]$$

Thus in the absence of any plastic deformation, the strain distribution is

$$e = (\Sigma^*/E^*) + \kappa^*h^*. \quad [27]$$

The total moment of the system

$$\int_{-H^*/2}^{H^*/2} h^* \sigma(h^*, t^*) dh^*, \quad [28]$$

will change with time from the value \mathbf{m} obtained from the solutions to (4) detailed in the previous section, dependent on solutions to the system (26), which is complete when the specific forms for $\kappa^*(t^*)$ from the beam calculation are assumed. Our assumption that $\kappa^*(t^*)$ does not change under relaxation precludes us from imposing any constraints on the applied couple.

We define non-dimensionalised quantities

$$\begin{aligned} \sigma^* &= Y^*\sigma, & t^* &= T^*t, & h^* &= H^*h, & \eta &= Y^*/E^*, & [29] \\ \phi^* &= \phi/(T^*Y^*), & \Sigma^* &= Y^*\Sigma, & V^* &= (H^*/T^*)V, \end{aligned}$$

with $T^* = \pi R^*/2V^*$ the time taken to pass over a quarter of the blade at a velocity V^* . With this rescaling the critical stress is unity, h spans the domain $[-1/2, 1/2]$ and the maximum possible time spent in contact by the element of the ribbon and the blade is 1. The model now has the form

$$e(h, t) = \bar{e}(t) + \kappa(t)h, \quad [30a]$$

$$e_t = \eta\sigma_t + \phi(\sigma - 1)H(\sigma - 1), \quad [30b]$$

$$\int_{-1/2}^{1/2} \sigma(h, t) dh = \Sigma. \quad [30c]$$

At low loads with point contact between ribbon and blade and $\theta_e = \pi/4$, the curvature distribution takes the form

$$\kappa(t) = \begin{cases} \sqrt{48\Sigma\eta} \operatorname{sech}(-Vt\sqrt{12\Sigma\eta} + L_0) & \text{if } t \leq 0, \\ \sqrt{48\Sigma\eta} \operatorname{sech}(Vt\sqrt{12\Sigma\eta} + L_0) & \text{if } t > 0. \end{cases} \quad [31]$$

In the case of line contact, the time spent passing over half the contact region is $t_b = s_0/V$, with $2s_0$ the total arclength of the strip in contact with the blade, and

$$\kappa(t) = \begin{cases} \sqrt{48\Sigma\eta} \operatorname{sech}((V(-t) - s_0)\sqrt{12\Sigma\eta} + L_0) & \text{if } t < -t_b, \\ \kappa_b & \text{if } -t_b \leq t \leq t_b, \\ \sqrt{48\Sigma\eta} \operatorname{sech}((Vt - s_0)\sqrt{12\Sigma\eta} + L_0) & \text{if } t > t_b. \end{cases} \quad [32]$$

For later reference, we note that (30) can be reformulated in terms of the evolving stress as

$$\eta\sigma_t = \kappa_t h + \phi \left[\int_{-1/2}^{1/2} (\sigma - 1)H(\sigma - 1)dh - (\sigma - 1)H(\sigma - 1) \right] \quad [33]$$

with $\int_{-1/2}^{1/2} \sigma dh = \Sigma$ where $\kappa = 0$. Alternatively, in terms of the evolving plastic strain $e_p = e - \eta\sigma$, (30) becomes

$$e_{p,t} = \frac{\phi}{\eta} f[e_p]H(f[e_p]), \quad [34]$$

$$f[e_p] \equiv \int_{-1/2}^{1/2} e_p dh + \kappa h + \eta(\Sigma - 1) - e_p,$$

from which the uniform strain is determined via

$$\bar{e} = \int_{-1/2}^{1/2} e_p dh + \Sigma\eta. \quad [35]$$

Determining the onset of yielding. In the absence of any plastic deformation, with $\sigma = e/\eta$ and $\bar{e} = \eta\Sigma$, the maximum stress occurs at $h = 1/2$ whilst the element is on the blade, where the curvature takes its maximum value

$$\kappa_0 = \min\left(\kappa_b, \sqrt{48\Sigma\eta} \sin(2\theta_e)\right). \quad [36]$$

There can be plastic deformation only if

$$\frac{\eta\Sigma + \kappa_0/2}{\eta} \geq 1 \quad [37]$$

which defines the minimal load $\Sigma_0 = 1 - \kappa_0/(2\eta)$ for the onset of curling. If this condition is met then there will be a time $-t_{min}$ ($t_{min} \geq 0$) at which (37) first becomes an equality. For point contact this value can be obtained by solving

$$\eta\Sigma + \kappa(t_{min})/2 = \eta, \quad [38]$$

$$\kappa(t_{min}) = \sqrt{48\Sigma\eta} \operatorname{sech}\left(Vt_{min}\sqrt{12\Sigma\eta} + L_0\right).$$

For line contact (37) is satisfied with $\kappa = \kappa_b$ and t_{min} satisfies

$$\eta\Sigma + \kappa(t_{min})/2 = \eta, \quad [39]$$

$$\kappa(t_{min}) = \sqrt{48\Sigma\eta} \operatorname{sech}\left((Vt_{min} - s_0)\sqrt{12\Sigma\eta} + L_0\right),$$

$$s_0 = \theta_0/\kappa_b.$$

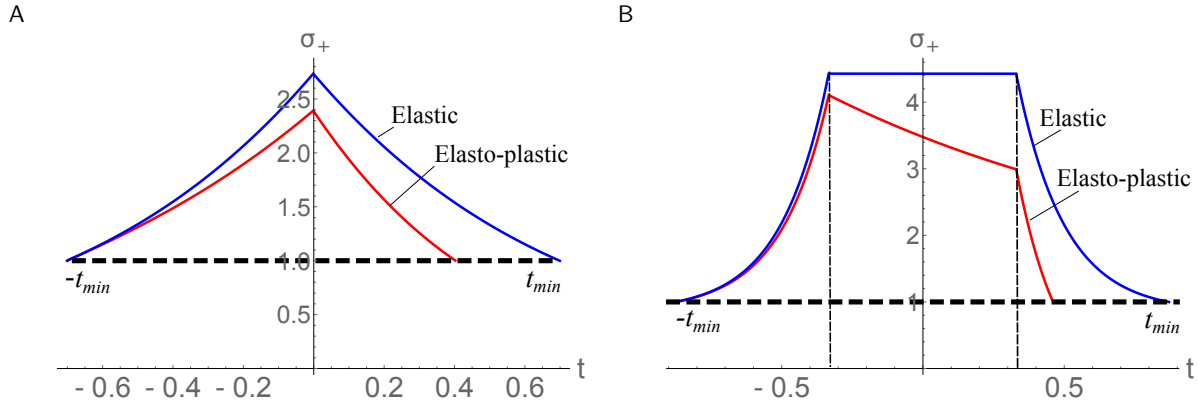


Fig. S7. (A) Typical solution for $\sigma_+ = \sigma(1/2, t)$ in the case of point contact, along with the elastic stress in the absence of any plastic deformation. The applied load is $\Sigma^* = 2$ MPa. (B) Typical solution for σ_+ in the case of line contact and symmetric elastic stress distribution, in the absence of plastic deformation. The applied load is $\Sigma^* = 30$ MPa. The other parameters are $t_p^* = 0.35$ s, $Y^* = 35$ Mpa, $E^* = 2.5$ GPa, $H^* = 100$ μ m and $R^* = 1$ mm.

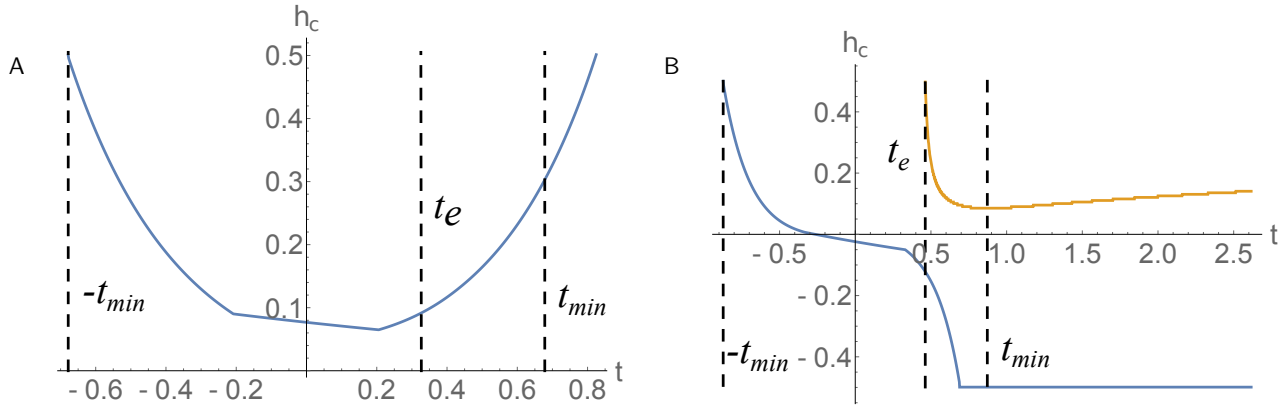


Fig. S8. Plots of the critical line $h_c(t)$ (blue line) (for which $\sigma(h_c) = 1$) for solutions to (34) corresponding to cases (A) and (B) in Fig. 3 in the main paper. The second critical line shown in (B) (orange line) is h_{2c} , which emerges when there is relaxation below the midline. The parameters used in the calculations are $t_p^* = 0.35$ s, $Y^* = 35$ Mpa, $E^* = 2.5$ GPa, $H^* = 100$ μ m and $R^* = 1$ mm, with applied loads $\Sigma^* = 10$ MPa in (A), and $\Sigma^* = 30$ MPa in (B).

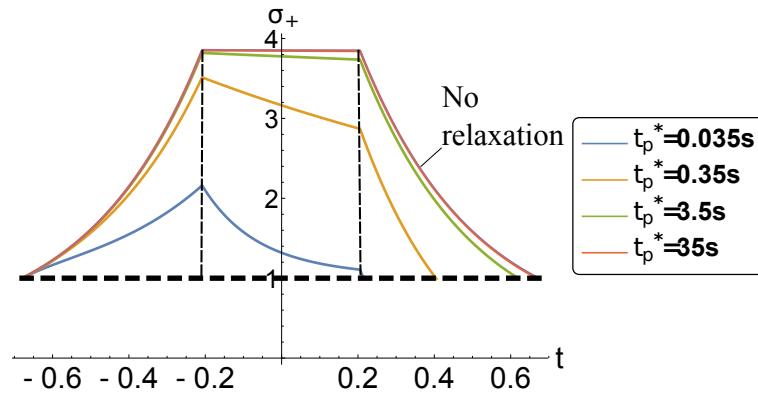


Fig. S9. Time-dependence of upper-surface stress σ_+ when the ribbon in line contact with the blade, for different values of the relaxation time t_p^* shown in the legend. Increasing the value of $t_p^* = 0.35$ s used in Fig. 3 in the main paper by an order of magnitude causes the stress to decay more rapidly to unity, while lowering t_p^* reduces the plastic deformation towards the purely elastic limit. The parameters used in the calculations were $\Sigma^* = 10$ MPa, $Y^* = 35$ Mpa, $E^* = 2.5$ GPa, $H^* = 100$ μ m and $R^* = 1$ mm.

Relaxation to a coiled ribbon. After integration of (34) or (33) to a time t_f at which the ribbon element is straight and stress relaxation is complete, yielding a residual plastic strain distribution $e_p(h)$, the load is removed from the ribbon and we

assume it relaxes elastically (ignoring gravity) to form a coil with the ribbon's centreline having a constant curvature κ_c , average strain \bar{e}_c and hence stress $\sigma(h) = (\bar{e}_c + \kappa_c h - e_p(h))/\eta$. Enforcing a force and moment balance under zero applied load

and couple,

$$\int_{-1/2}^{1/2} \sigma \, dh = 0, \text{ and } \int_{-1/2}^{1/2} h\sigma \, dh = 0, \quad [40]$$

gives \bar{e}_c and κ_c , as functions of the Σ and the material parameters.

Numerical results. We solve (34) numerically as an initial value problem, keeping track of the internal free boundary $h = h_c$ at which $\sigma = (e - e_p)/\eta = 1$. The initial condition of no plastic yielding is $e_p(h, -t_{min}) = 0$ for all h , with t_{min} obtained by solving either (38) or (39).

Typical time-dependent relaxation of material is illustrated by tracking the upper surface stress $\sigma_+ \equiv \sigma(1/2, t)$. This is shown in Fig. S7A (point contact) and B (line contact) for parameters representative of those used to obtain the experimental fits (Fig. 2 in the main paper). There is a significant decrease in σ_+ relative to the unyielded value, starting at $-t_{min}$ and ending at a time t_e when σ^+ drops below unity.

The time-varying stress distributions across the ribbon cross-section show two regimes, distinguished by the behaviour of the free boundary h_c . Snapshots of typical cases from each family are shown in Fig. 3 in the main paper, along with the associated curvature distributions. In both cases the shaded region indicates the yield surface of the material. The relaxation of σ from its value in the absence of yielding, $\sigma_e \equiv e/\eta$, drives h_c from $h = 1/2$ towards the lower boundary in order to maintain stress balance (as depicted in Fig. S8A). The rate at which h_c migrates is driven by the time varying curvature distribution. The rise of $\kappa(t)$ prior to the ribbon element reaching the blade drives a rapid drop of h_c towards the ribbon mid-line. On the blade, the curvature is fixed and h_c decreases linearly. For case A, representing lower axial loads, after leaving the blade the curvature decreases to zero and h_c rises rapidly towards $h = 1/2$ at $t = t_e$ (Fig. S8A). For case B, representing higher axial loads (Fig. 3B in the main paper), the yield surface at $h = h_c$ drops below the mid-line whilst on-blade, and after leaving the blade instead falls rapidly towards $h = -1/2$. In addition, a second interface at $h = h_{2c}$ (where $\sigma(h_{2c}) = 1$) appears (see Fig. 3B(iv) in the main paper). It originates at $h = 1/2$ and rapidly drops towards the mid-line (driven by the rapidly lowering curvature). Once the curvature has dropped to a significantly low value there is an almost uniform yielding and h_{2c} rises towards $h = 1/2$ in order to preserve the total stress (see panels (iv) and (v) of Figs. 3 and S8B).

In the low-load regime the domain h_c remains above the midline and any plastic relaxation is restricted to the upper half of the ribbon. In the high-load regime plastic relaxation extends to the lower half of the domain. The yielding of the upper layer of the material, mainly occurring pre- and on-blade, leads to a plastic strain gradient. Yielding of the lower layer, if present, occurs off-blade and leads to a more uniform distribution of plastic yielding, decreasing the equilibrium curvature observed in Fig. 2.

Varying the relaxation time. The plastic relaxation timescale t_p^* is related to the transit time over the ribbon $T^* = \pi R^*/2V^*$ though $t_p^*/T^* = \eta/\phi$. For the 1 mm blade and $V^* = 4.9$ mm/s used in the experiments, $T^* \approx 0.32$ s and $t_p^* = T^*$ for $\phi \approx 0.035$, the value used in Fig. S7. A significant decrease in the amount of plastic yielding occurs when t_p^* increases (i.e. ϕ decreases) by one and two orders of magnitude (Fig. S9). Consequently, for the model to predict significant plastic deformation we require that the plastic yielding timescale is not much greater than the time spent by the material element on the blade.

Fig.

Net axial strain. S10A shows the net axial strain $\bar{e}(t_f)$ as a function of Σ for various blade curvatures, where t_f is the time at which yielding of the ribbon element has ceased. $\bar{e}(t_f)$ increases monotonically with Σ and κ_b . For the same parameters, Fig. S10B shows $E_d \equiv e_p(1/2, t_f) - e_p(-1/2, t_f)$, the difference between the final permanent deformation of the upper and lower surfaces. The difference E_d has a gradient which alters sign at some critical load Σ_c .

In both cases three distinct regimes can be identified. For low loads the gradient of increase is relatively sharp, coinciding with the ribbon having point contact with the blade. For point contact the maximum curvature κ_0 increases as the square root of the load (see equation (23)), and this rapid change in curvature seems to drive the relatively steep initial gradient in each variable. The gradient then falls as the load increases and the ribbon comes into line contact with the blade, limiting the maximum permissible curvature to be κ_b . For medium to high loads (dependent on the blade curvature), yielding of the lower part of the ribbon accelerates the growth of $\bar{e}(t_f)$, increasing the gradient of the curve significantly. This is also the domain in which E_d falls with increasing load, due to yielding of the lower layer of the ribbon ($e_p(1/2, t_f)$ is fixed but $e_p(-1/2, t_f)$ increases, see Fig. 3B (iv) and (v) in the main paper). The dependence of net axial strain on load mirrors experimental observations (Fig. S2).

Asymptotic solution with rapid stress relaxation. Further insight into the model emerges in the limit of rapid stress relaxation, when a boundary-layer structure emerges in the stress field. We demonstrate how, when the yield surface h_c is advancing downwards into the ribbon (as in examples (i-iii) of Fig. 3 in the main paper), the curvature-load relation can be approximated analytically.

Returning to (33), we write $\sigma = 1 + F(h)$ with $F < 0$ in $-\frac{1}{2} < h < h_c(t)$ and $F > 0$ in $h_c(t) < h < \frac{1}{2}$. A local expansion near $h = h_c$ is obtained by writing $h = h_c + \xi$ and setting $F = F^\pm(\xi, t)$ in each region so that (33) becomes

$$\eta(F_t^+ - h_{c,t}F_\xi^+) = \kappa_t(h_c + \xi) + \phi [I - F^+], \quad [41a]$$

$$\eta(F_t^- - h_{c,t}F_\xi^-) = \kappa_t(h_c + \xi) + \phi I, \quad [41b]$$

$$I \equiv \int_0^{1/2-h_c} F^+ \, d\xi. \quad [41c]$$

Then setting $F^\pm(\xi) = \alpha^\pm(t)\xi + \frac{1}{2}\beta^\pm(t)\xi^2 + \dots$ and expanding in ξ we obtain conditions on the coefficients as follows. At $O(1)$,

$$-\eta\alpha^\pm h_{c,t} = \kappa_t h_c + \phi I \quad [42]$$

so that if $h_{c,t} \neq 0$ then $\alpha^\pm = \alpha(t)$, say. The purely elastic response of the unyielded region is represented by $F^- = \kappa\xi/\eta$, which requires

$$0 = (\kappa h_c)_t + \phi I \quad [43]$$

and hence $\alpha = \kappa/\eta$, $\beta^- = 0$, etc. At $O(\xi)$, we find that

$$\beta^+ = \frac{\phi\kappa}{\eta^2 h_{c,t}} \quad (h_{c,t} \neq 0) \quad [44]$$

and so on. The ratio α/β identifies a lengthscale $L \equiv \eta|h_{c,t}|/\phi$.

When stress relaxation is rapid, so that $t_p^* \ll T^*$ and $\eta \ll \phi$, L is small, indicating the presence of a boundary layer at the base of the yielded region near $h = h_c$. An outer solution in the yielded region is obtained by returning to $\eta F_t = \kappa_t h + \phi [I - F]$ and neglecting the time derivative, so that $F = (\kappa_t h/\phi) + I$. (The outer solution in the yielded region, and the solution in

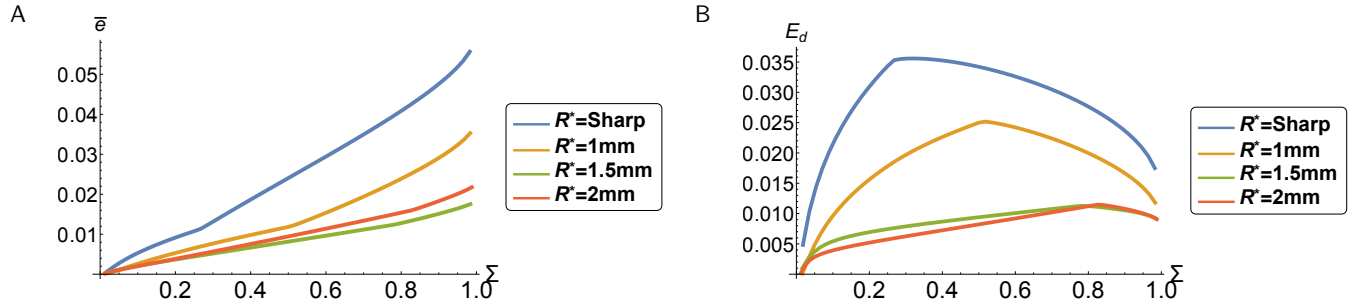


Fig. S10. (A) Final axial stretch $\bar{\epsilon}(t_f)$ as a function of applied load Σ . (B) The strain difference between upper and lower surfaces $E_d = e_p(1/2, t_f) - e_p(-1/2, t_f)$ as a function of load. The calculations were performed with the same parameter values as in Fig. 2B in the main paper.

the unyielded region, are both linear in the transverse coordinate, consistent with numerical predictions of the stress in cases (i)-(iii) of Fig. 3 in the main paper.) We can then estimate the integral by neglecting any contribution from the boundary layer, so that

$$I \approx \int_{h_c}^{1/2} \left(I + \frac{\kappa_t h}{\phi} \right) dh \quad [45]$$

from which it follows that $I = (\kappa_t/2\phi)(\frac{1}{2} - h_c)$. Combining this with (43) implies $0 = \kappa_t(h_c + 1/2) + 2\kappa h_{c,t}$ and hence $\kappa(h_c + \frac{1}{2})^2 = C^2$ for some constant C . Thus the location of the yield point is controlled directly by the magnitude of the curvature, as long as the curvature is evolving. The onset of yield is given by the condition (37), when the stress first reaches unity at $h_c = 1/2$, i.e. $\sigma = \Sigma + \kappa h/\eta = 1$ at $h = 1/2$. Thus $\kappa = 2\eta(1 - \Sigma)$ when $h_c = 1/2$ and so

$$\kappa(h_c + \frac{1}{2})^2 = 2\eta(1 - \Sigma). \quad [46]$$

Thus the yield point reaches the ribbon midline if $\kappa \geq 8\eta(1 - \Sigma)$, but never reaches the opposite side of the ribbon while κ is increasing.

The outer solution in the yielded region therefore approaches the limit $F^+ = (\kappa_t h_c/\phi) + I = (\kappa_t/2\phi)(h_c + \frac{1}{2})$ as $\xi \rightarrow 0$. The boundary layer is described by returning to (41a) and discarding the time derivative F_t^+ . Writing $\xi = L\hat{\xi}$ and $F^+ = (\kappa_t/\phi)\hat{F}(\hat{\xi})$, and noting that $h_{c,t}/|h_{c,t}| = -1$ as the yield point advances into the ribbon, (41a) reduces to

$$\hat{F}_{\hat{\xi}} = \frac{1}{2}(h_c + \frac{1}{2}) - \hat{F} \quad [47]$$

for $L \ll 1$. This has the solution $\hat{F} = \frac{1}{2}(h_c + \frac{1}{2})(1 - e^{-\hat{\xi}})$. Its outer limit matches the inner limit of the outer solution. The inner limit $\hat{F} = \frac{1}{2}(h_c + \frac{1}{2})(\hat{\xi} - \frac{1}{2}\hat{\xi}^2 + \dots)$ recovers $F^+ = \alpha\xi + \frac{1}{2}\beta^+\xi^2 + \dots$ as required.

To interpret (46), we substitute the full solution for F^\pm (ignoring the short boundary layer) into the force balance (30c). This yields

$$\Sigma = \frac{\kappa}{2\eta}(\frac{1}{2} + h_c)^2 + \frac{\kappa_t}{2\phi}(\frac{1}{2} - h_c) \quad [48]$$

representing elastic and viscous contributions from the unyielded and yielded portions of the ribbon respectively. For rapid relaxation, with $\kappa_t/\phi \ll \kappa/\eta$ (off-blade, this this condition becomes $V\sqrt{\Sigma\eta} \ll \phi/\eta$ using (31, 32)), the elastic contribution dominates and recovers (46). Because of this, once the curvature reaches its on-blade plateau, h_c becomes stationary and the stress in the yielded region relaxes to unity. This will cause an adjustment to the position of h_c . However this can

be neglected as the force balance does not depend on the load carried in the yielded region to leading order.

We can now use the outer solution to calculate the residual curvature κ_c , for cases in which the ribbon yields only in the upper half of its cross-section. Letting e_p be the irreversible strain, the moment balance (40) gives

$$\int_{-1/2}^{1/2} \kappa_c h^2 dh = \int_{-1/2}^{1/2} e_p h dh, \quad [49]$$

where, we recall $e_{p,t} \equiv \phi(\sigma - 1)H(\sigma - 1)$. Thus

$$\kappa_{c,t} = 12 \int_{h_c}^{1/2} \phi F dh = \kappa_t \int_{h_c}^{1/2} (h^2 + \frac{1}{4}h - \frac{1}{2}hh_c) dh \quad [50]$$

which reduces to $\kappa_{c,t} = \kappa_t(\frac{1}{2} - h_c)(\frac{7}{4} + 2h_c + h_c^2)$. But (46) implies

$$h_c = -\frac{1}{2} + \sqrt{\frac{2\eta(1 - \Sigma)}{\kappa}} \quad [51]$$

so we may write $\kappa = 2\eta(1 - \Sigma)K$, $\kappa_c = 2\eta(1 - \Sigma)K_c$ and consider K rising from 1 at the onset of yield to a value K_m representing the plateau κ_{\max} (23) in curvature associated with line contact over the blade. Then integrating over the time interval over which the ribbon curvature rises, and using h_c to parametrize time, we obtain

$$K_c = \int_{-1/2+K_m^{-1/2}}^{1/2} \frac{(1 - 2y)(\frac{7}{4} + 2y + y^2)}{(y + \frac{1}{2})^3} dy \quad [52]$$

$$= \left[-2y - \frac{1}{(y + \frac{1}{2})^2} \right]_{-1/2+K_m^{-1/2}}^{1/2} \quad [53]$$

$$= K_m + \frac{2}{K_m^{1/2}} - 3 \quad [54]$$

This can be re-expressed as

$$\frac{\kappa_c}{\kappa_{\max}} = 1 + 2 \left(\frac{2\eta(1 - \Sigma)}{\kappa_{\max}} \right)^{3/2} - 3 \left(\frac{2\eta(1 - \Sigma)}{\kappa_{\max}} \right) \quad [55]$$

giving a curve that rises monotonically from $(\Sigma, \kappa_c) = (1 - \kappa_{\max}/(2\eta), 0)$ (where $h_c = \frac{1}{2}$) to $(1 - \kappa_{\max}/(8\eta), \kappa_{\max}/2)$ (where $h_c = 0$). For a ribbon in line contact with the blade, $\kappa_{\max} = \kappa_b \equiv \epsilon$, whereas in point contact $\kappa_f = \sqrt{48\Sigma\eta} \equiv \sqrt{48\epsilon\Sigma/\mathcal{C}}$ when $\theta_e = \pi/4$. This analysis takes no account of the reduction in κ_c that occurs at high loads if the yield surface enters the lower half of the ribbon. The estimate of maximum curvature $\kappa_{\max}/2$ overestimates the measured maxima in Fig. 2A, suggesting that stress relaxation effects are significant in experiments.

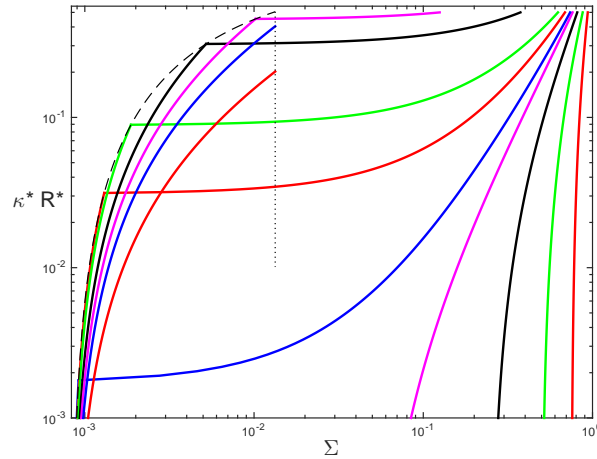


Fig. S11. The rising segment of the curvature versus load curve (55) for $C = 0.5, 1, 1.5, 1.9, 2.1, 2.5, 3, 5, 7, 10, 20$ (right to left) on a log scale for $C/\epsilon = 100$. For $2 < C < 8$ the curves have a kink marking the transition between point and line contact; the kink lies on the dashed curve. For $C > 8$ the curve terminates at a location on the dotted line $\Sigma = 4\epsilon/3C$.

The curvature-load relation in analytic form. Nevertheless, it is revealing to examine (55) and its dependence on the model’s governing parameters, particularly the curling number $C = \epsilon/\eta$. For line contact, with $0 < C < 2$, (55) becomes

$$\kappa^* R^* = 1 + 2 \left(\frac{2}{C} (1 - \Sigma) \right)^{3/2} - \frac{6}{C} (1 - \Sigma), \quad 1 - \frac{1}{2}C < \Sigma < 1 - \frac{1}{8}C. \quad [56]$$

Thus curves differ for different curling numbers C : thinner ribbons with smaller C curl over narrower ranges of loads. For $C > 2$, point contact takes place at low loads. Writing $\Sigma = \epsilon \hat{\Sigma}$ and neglecting terms of $O(\epsilon)$, the line contact relation (56) terminates close to zero load (at $\hat{\Sigma} = C/48$) with $\kappa^* R^* \approx 1 + 2^{5/2} C^{-3/2} - (6/C)$. This function rises from 0 at $C = 2$ to $1/2$ at $C = 8$. The curvature-load curve rises from zero to this value according to

$$\kappa^* R^* \approx \frac{1}{C} \left(\sqrt{48 \hat{\Sigma} C} + \left(\frac{2^6}{3C \hat{\Sigma}} \right)^{1/4} - 6 \right), \quad \frac{1}{12C} < \hat{\Sigma} < \frac{C}{48} \quad [57]$$

for $2 < C < 8$ (again assuming small ϵ). For $C > 8$ the line contact solution is no longer relevant and there is point contact along the entire rising curvature-load curve. The threshold $\kappa_{\max} = 8\eta$ becomes $\hat{\Sigma} = 4/(3C)$, and the curve in (57) is confined to $1/12 < \hat{\Sigma} C \equiv E^* \Sigma^*/Y^{*2} < 4/3$ (a range independent of H^* and R^*), rising to maximum curvature $\kappa^* R^* = 4/C$, i.e. $\kappa^* = 4Y^*/H^*E^*$ (independent of R^*). Further increases in C shrink the range of loads over which curvature is generated and reduce the maximum curvature.

Fig.

S11 shows how the predicted rising branch of the curvature-load relationship depends on ϵ and C , varying each while holding $C/\epsilon = E^*/Y^*$ constant. Thicker ribbons can be curled at lower loads but curl less when very thick. The graph shows how the curvature-load curve (55) transitions between self-similar forms (56) and (57) when the ribbon is respectively in pure line ($C < 2$) or pure point ($C > 8$) contact with the blade.

1. Young, R.J. & Lovell, P.A. (2011) Introduction to polymers (3rd ed.), CRC Press.
2. Wilkes, C. E. (2005) PVC Handbook, Hanser Verlag.
3. Antman, S. S. (2005), Nonlinear Problems of Elasticity (Chapter 8), Springer.
4. Pikey, W. D. (2001) Analysis and Design of Elastic Beams. Wiley and Sons.
5. Timoshenko, S. P. (1921) On the correction factor for shear of the differential equation for transverse vibrations of bars of uniform cross-section. The London, Edinburgh, and Dublin Philosophical Magazine and Journal of Science 41, 744-746.
6. Kehrbaum, S. & Maddocks, J. H. (1997) Elastic rods, rigid bodies, quaternions and the last quadrature. Proc. R. Soc A. 355, 2117-2136.
7. Lubliner, J. (2008) Plasticity theory. Dover.